Doctoral Thesis in Nuclear Engineering

Decision Tree Insights Analytics (DTIA): An Explainable AI Framework for Severe Accident Analysis

KARIM HOSSNY

KTH ROYAL INSTITUTE OF TECHNOLOGY

Decision Tree Insights Analytics (DTIA): An Explainable AI Framework for Severe Accident Analysis

KARIM HOSSNY

Academic Dissertation which, with due permission of the KTH Royal Institute of Technology, is submitted for public defence for the Degree of Doctor of Philosophy on Friday the 16th of January 2026, at 10:00 a.m. in FB51, Roslagstullsbacken 21, AlbaNova University Centrum, Stockholm, Sweden.

Doctoral Thesis in Nuclear Engineering
KTH Royal Institute of Technology
Stockholm, Sweden 2025

TRITA-SCI-FOU 2025:78
ISBN 978-91-8106-509-1

Printed by: Universitetsservice US-AB, Sweden 2025

*This Dissertation is dedicated to my brother, **Mo Hossny**, who has been there through every up and down stage of my PhD journey and to my emotional support ROCK, **Kristen Fagerstrom** (Kristen Johnston), on whom I leaned, and she was always there to celebrate good news and, more importantly, pick up the pieces after bad news.*

Abstract

In nuclear reactor safety analysis, we label an accident as severe once a partial core meltdown and material relocation begin. Researchers use simulation tools such as ANSYS and MELCOR to study these events safely, producing vast and complex datasets. In this work, we applied machine learning explainability and interpretability to extract insights from severe accident simulations for the Nordic boiling water reactor (BWR) through five iterative studies. First, we examined the explainability of the decision tree classification algorithm to distinguish between accident types using time-wise pressure vessel external temperature. Second, we generalised the model to create a more statistically robust and generic framework, introducing the open-source Decision Tree Insights Analytics (DTIA) framework (https://github.com/KHossny/DTIA), which combines explainability, interpretability, and statistical robustness. Third, we applied DTIA to high-dimensional MELCOR COR package data for a station blackout combined with a loss-of-coolant accident (SBO + LOCA) in a Nordic BWR, revealing new findings. Fourth, we used DTIA to compare structural variables of the reactor pressure vessel lower head under SBO and SBO + LOCA conditions. Finally, we coupled DTIA with K-Means clustering to address its need for labelled data, uncovering previously overlooked events such as canister melting. We concluded that the patterns identified by machine learning in mapping inputs to outputs can uncover insights that were previously overlooked, particularly in high-dimensional and complex datasets.

Keywords

Explainable AI, Decision Tree Insights Analytics (DTIA), Nuclear Severe Accidents Analysis, Decision Tree Classification, Reactor Pressure Vessel Failure.

Sammanfattning

Inom analysen av kärnreaktorsäkerhet betecknar vi en olycka som allvarlig när en partiell härdsmälta och materialomplacering inleds. Forskare använder simuleringsverktyg som ANSYS och MELCOR för att studera dessa händelser på ett säkert sätt, vilket genererar stora och komplexa datamängder. I detta arbete tillämpade vi maskininlärningens förklarbarhet och tolkbarhet för att utvinna insikter från simuleringar av allvarliga olyckor för den nordiska kokvattenreaktorn (BWR) genom fem iterativa studier. För det första undersökte vi förklarbarheten hos beslutsträdsklassificeringsalgoritmen för att skilja mellan olyckstyper baserat på tidsberoende yttre temperatur på reaktortanken. För det andra generaliserade vi modellen för att skapa ett mer statistiskt robust och generiskt ramverk och introducerade det öppna ramverket **Decision Tree Insights Analytics (DTIA)** (https://github.com/KHossny/DTIA), som kombinerar förklarbarhet, tolkbarhet och statistisk robusthet. För det tredje tillämpade vi DTIA på högdimensionella data från MELCOR:s COR-paket för ett totalt strömavbrott kombinerat med ett kylvätskeförlustscenario (SBO + LOCA) i en nordisk BWR, vilket avslöjade nya fynd. För det fjärde använde vi DTIA för att jämföra strukturella variabler i reaktortankens nedre del under SBO- och SBO + LOCA-förhållanden. Slutligen kopplade vi DTIA till K-Means-klustring för att hantera behovet av märkta data, vilket avslöjade tidigare förbisedda händelser som smältning av kapseln. Vi drog slutsatsen att de mönster som identifieras av maskininlärning vid koppling mellan indata och utdata kan avslöja insikter som tidigare förbises, särskilt i högdimensionella och komplexa datamängder.

Nyckelord
Förklarbar AI, Decision Tree Insights Analytics (DTIA), Analys av allvarliga kärnkraftsolyckor, Beslutsträdsklassificering, Haveri av reaktortryckkärl.

Acknowledgements

The number of people who helped me reach this point can't be covered in a page or two acknowledgement section. However, this section includes the highlights of the magnificent people without whom this moment wouldn't have come.

First, I would like to express my gratitude to my supervisors, Walter Villanueva and Chong Qi. Walter isn't just a supervisor; he is also a friend. He never doubted me, even when an idea was rejected more than once. His supervision framework relied on combining my experience and knowledge with his to create something better than what I had. Chong made things easier by stepping in to resolve logistical challenges. For that, I am thankful to both of them, as well as to Torbjörn Back, who, as head of the Nuclear Science and Engineering (NSE) division, handled administrative challenges professionally and efficiently. Also, I would like to thank Pär Olsson, who, as head of the physics department, helped overcome many challenges that would have been much more difficult without his intervention. Finally, I would like to thank Pavel and Dmitry for the knowledge I gained during my work with them.

Second, my colleagues and friends at the NSE, with whom I shared the same journey, had numerous discussions that significantly improved the working conditions and the work presented in this dissertation. Among them were Ibrahim and Fares, who welcomed me to the division when I was first transferred there. Then, of course, we have Yi Meng Chan, with whom I had numerous machine learning discussions, as well as many more that I can't mention in this section. Of course, Vivian Peters has supported me in various ways over the past year. Last but not least, I would like to thank Hongdi and Boshen, who not only welcomed me at KTH when I first joined but also assisted me with onboarding, as demonstrated in this dissertation; some of the work builds upon Hongdi’s work.

Finally, my friends and family, whom I know I can always rely on, are there to support me. I would like to thank my family for their support and encouragement from overseas. This includes my mom, dad, Ahmed Hossny, Mostafa Hossny and of course Rowan Badran, who was there since it all started. My friends, I'm at a loss for words to describe how much they've helped me through this journey. Starting with Ahmed and Mahmoud El-Tourky (yes, brothers), who helped me with the paperwork when I relocated to Sweden. Eslam, Aya, Ibrahim, Dina, Ashraf, Hala, Aboud, Aya (note: different person), and their families, who, despite being spread across three continents, were always there. Of course, El-Awwad (Mr El-Awwad), Tarek (El-Tarook), Akl and Loay, who literally travelled all the way to Stockholm to help me go through the tough times. Last but not least, I would like to thank Sara and Rayhana, who helped me get by when I first relocated. Of course, my other family here in Stockholm, Moody, Adam, Katherin, Kajsa, Lamia, Daniil, Monika and Yaz.

As mentioned at the beginning of this section, the people who helped make this moment possible are numerous and can’t be covered in a single section. It also goes without saying that I am thankful for all the fruitful discussions with the co-authors and various collaborators.

List of publications included in this dissertation

Paper 1: **K. Hossny**, W. Villanueva, HD Wang, “Distinctive Physical Insights Driven from Machine Learning Modelling of Nuclear Power Plant Severe Accident Scenario Propagation”, **Nature Scientific Reports**, 2023.

Paper 2: **Karim Hossny**, Mohamed Hossny, Antony Cougnoux, Loay Mahmoud, Walter Villanueva, “Decision Tree Insights Analytics (DTIA) Tool: an Analytic Framework to Identify Insights from Large Data Records Across Fields of Science”, **Machine Learning: Science and Technology**, 2024.

Paper 3: **Karim Hossny** and Walter Villanueva, “Nuclear Reactor Core Relocation During Severe Accident using Decision Tree Insights Analytics (DTIA)”, **[Submitted to Energy and AI Journal]**.

Paper 4: **Karim Hossny**, Walter Villanueva and Mostafa ElNaggar, “Objective Segmentation of Nuclear Reactor Pressure Vessel Structural Analysis Variables using Decision Tree Insights Analytics (DTIA)”, **[Submitted to Nuclear Science and Techniques Journal]**.

Paper 5: **Karim Hossny** and Walter Villanueva, “Towards Objectivity in Nuclear Severe Accidents Analysis Via K-Means Clustering and Decision Tree Insights Analytics (DTIA) Framework”, International Congress on Advances in Nuclear Power Plants **(ICAPP 2025)**, Antibes, France, 2025.

Authors Contributions

Paper 1:

Karim Hossny: conceptualisation, method development, coding, data cleaning and preparation, data analysis, data interpretation, discussion, writing original drafts, revising draft versions, submission and addressing review comments.

Walter Villanueva: conceptualisation, method development, data interpretation, discussion, revising draft versions and Supervision.

Hongdi Wang: data interpretation, discussion and revising draft versions.

Paper 2:

Karim Hossny: conceptualisation, method development, coding, data cleaning and preparation, data analysis, data interpretation, discussion, writing original drafts, revising draft versions, submission and addressing review comments.

Mohammed Hossny: conceptualisation, method development, coding and revising draft versions.

Antony Cougnoux: data interpretation, discussion, writing original drafts and revising draft versions.

Loay Mahmoud: data interpretation, discussion, writing original drafts and revising draft versions.

Walter Villanueva: conceptualisation, method development, data interpretation, discussion, revising draft versions and Supervision.

Paper 3:

Karim Hossny: conceptualisation, method development, coding, data cleaning and preparation, data analysis, data interpretation, discussion, writing original drafts and revising draft versions.

Walter Villanueva: data interpretation, discussion, revising draft versions, and supervision.

Paper 4:

Karim Hossny: conceptualisation, method development, coding, data cleaning and preparation, data analysis, data interpretation, discussion, writing original drafts and revising draft versions.

Walter Villanueva: data interpretation, discussion, revising draft versions, and supervision.

Mostafa ElNaggar: data interpretation, discussion and revising draft versions.

Paper 5:

Karim Hossny: conceptualisation, method development, coding, data cleaning and preparation, data analysis, data interpretation, discussion, writing original drafts, revising draft versions, submission and addressing review comments.

Walter Villanueva: data interpretation, discussion, revising draft versions, and supervision.

List of publications not included in this dissertation

1. **K. Hossny** and Walter Villanueva, Analysing Nuclear Reactor Severe Accident Time-Wise Propagation using DTIA, ANS Annual Conference, **American Nuclear Society**, 2025.
2. Marina R. Abdelnour, Juntao Liu, **K. Hossny**, A. M. Wajid, Wenxin Li, Zhiyi Liu, "Prompt Gamma Neutron Activation Analysis: A Review of Applications, Design, Analytics, Challenges and Prospects", **Radiation Physics and Chemistry**, 2025.
3. **K. Hossny**, E. Salama, KF Mageed, YMZ Al-Bakhat, S. ElFiki, "Determination of the Full Energy Peak of HPGe Detector for Varying Soil Composition and Marinelli Beaker using Artificial Neural Networks", **Journal of Instrumentation**, 2022.

List of abbreviations

DTIA	Decision Tree Insights Analytics
DTC	Decision Tree Classification/Classifier
BWR	Boiling Water Reactor
SA	Severe Accident
SBO	Station Blackout Accident
LOCA	Loss of Coolant Accident
SBO + LOCA	Station Blackout and Loss of Coolant Accidents
RPV	Reactor Pressure Vessel
SML	Supervised Machine Learning
RF	Random Forest
TPC	True Positive Class
TNC	True Negative Class
FPC	False Positive Class
FNC	False Negative Class
NPC	Niemann-Pick Disease Type C1
AC	Astrocytes Cells
MC	Microglia Cells

EFPD	Fission Power and Decay Heat Generation in the Core
EMWR	Oxidation Heat Generation in the Core
DMH2	Hydrogen Production in the Core
DMH2_ZIRC	Hydrogen Production by Oxidation of Zircaloy
DMH2_SS	Hydrogen Production by Oxidation of Stainless Steel
MSS	Mass of Stainless Steel
MSSOX	Mass of Stainless Steel Oxide
MUO2	Mass of Uranium Dioxide
MZR	Mass of Zircaloy
PD MUO2	Particulate Debris Mass of Uranium Dioxide
PB MUO2	Particulate Debris Mass of Uranium Dioxide in the Bypass
TSS	Temperature of Stainless Steel
TSVC	Local Channel Fluid Temperature

CONTENTS

List of Figures

List of Tables

1 Introduction

Nuclear reactor safety focuses on analysing potential accident scenarios in nuclear power plants to ensure safe operation and minimise risks to personnel and the environment [1,2]. A single severe accident can have catastrophic consequences, which is why accident progression has been extensively studied since the start of nuclear power, covering initiating events, fault propagation, and the behaviour of neutronics, thermal hydraulics, and materials under accident conditions [3–24]. Due to the complexity of these phenomena, most studies have traditionally relied on computational modelling [25–32]. With advances in computational power, machine learning gained momentum across many fields and, more recently, in nuclear safety, where it has been applied to fault detection, transient analysis, and prediction accuracy enhancement through optimisation techniques. Research has demonstrated diverse approaches such as support vector machines with particle swarm optimisation for fault diagnosis, kernel principal component analysis for reducing false alarms, probabilistic regressors for predicting coolant pump seal leakage, dynamic Bayesian networks for failure detection, neural networks for corrosion and loose-part detection, and ensemble or hybrid methods for accident classification, sensor validation, and differentiation between equipment faults and cyber-attacks. Collectively, these efforts highlight the expanding role of machine learning in advancing reactor safety [33–53].

Supervised machine learning, in particular, has attracted significant attention due to computational advances that enabled large-scale data generation and training. These models are widely developed for regression tasks with numerical outcomes and classification tasks with categorical outcomes. Feature identification remains a central challenge, complicated by noise, dimensionality, and variance, and has been addressed through correlation analyses, physically motivated feature selection, and iterative testing with different feature sets [54,55]. Data pre-processing further improves model performance, ranging from simple normalisation to advanced transformations such as principal component analysis, independent component analysis, or linear discriminant analysis, and in more complex cases involving multiple sequential steps [56–59]. The introduction of grid search frameworks streamlined development by automating pre-processing, model selection, and evaluation, although at a high computational cost. These frameworks broadened accessibility to supervised learning and accelerated its application across research domains. More recently, the emergence of interpretability and explainability has sought to address the opaque nature of supervised models, especially in decision-making contexts. This area of research focuses on understanding how models reach specific outcomes, complementing predictive performance and revealing hidden patterns [60]. Work in supervised learning can therefore be divided into advancing new models or hybrid architectures and applying established methods to domain-specific problems.

Accident scenario propagation remains central to nuclear reactor safety, as it examines how accidents evolve and how radioactive material can be confined within containment. The challenge lies not in shutting down the chain reaction but in managing decay heat, which, if inadequately removed, can lead to core meltdown, vessel failure, and containment breach. Accident analysis guides reactor design, probabilistic safety assessments, and mitigation strategies, but the complexity of the system makes analysis inherently difficult. Modelling codes such as MELCOR and ASTEC simulate thousands of parameters, many of which are not equally significant. Selecting relevant parameters, therefore, depends heavily on expert judgement, leaving detailed analyses subjective despite regulatory standardisation of global propagation studies[29,32,61–64] . Machine learning has been adopted to address these issues, particularly supervised learning for regression and classification, applied both statically at specific time points and dynamically over time [65–69]. Despite these advances, interpretability and explainability remain underutilised. While predictive models focus on outcomes, interpretability seeks to clarify the decision-making process and uncover associations within the data. Linking these insights to physical knowledge provides a deeper understanding of accident progression beyond conventional prediction.

Understanding the progression of severe accidents is also vital for reactor pressure vessel behaviour, as core melting and corium relocation impose extreme thermal and mechanical loads that threaten the structural integrity. Analysing vessel behaviour under such conditions is crucial for developing management strategies, particularly for identifying failure modes, timing, and stress conditions [70–74]. Since experiments are impractical, computational modelling, especially the finite element method, has been the dominant tool. In parallel, machine learning has gained traction in structural analysis, where supervised models trained on experimental and synthetic data have been used to predict structural failure, and explainability techniques have been employed to identify parameters influencing outcomes. These approaches demonstrate how machine learning can complement computational tools and provide new insights into structural behaviour [75–78].

Severe accident research further benefits from unsupervised learning approaches, which remain relatively unexplored in nuclear applications [79]. While supervised learning has proven valuable for interpolation, surrogate model development, and accident classification, its black-box nature limits interpretability, leading most applications to prioritise accuracy over insights. Unsupervised clustering offers potential to address the subjectivity of accident analysis by grouping patterns in high-dimensional datasets without predefined outputs. When combined with explainable methods, such approaches can uncover hidden associations between parameters and accident outcomes, linking them to physical knowledge and revealing aspects of accident progression that traditional predictive models may overlook.

Due to the complexity of nuclear reactor systems and the high dimensionality of the generated data, as well as the interdisciplinary nature of severe accident propagation, traditional severe accident analysis by subject matter experts may overlook valuable insights worth investigating. Hence, in this work, we are proposing to complement the traditional analysis technique of severe accidents with an explainable and interpretable machine learning approach. We developed the Decision Tree Insights Analytics (DTIA) framework, which utilises the explainability of decision trees to analyse and extract insights from high-dimensional data generated by MELCOR and ANSYS for severe accident analysis.

1.1 Summaries of the Appended Papers

This dissertation consists of four main chapters:

- Chapter one: overview and an introduction to each of the papers listed in this dissertation, clarifying the purpose and the problem being solved in each study.
- Chapter Two: This chapter explains the evolution of the decision tree insights analytics (DTIA) framework, its applications on the different case studies and its evolution to be bootstrapped to the K-Means clustering algorithm.
- Chapter Three: This chapter includes the results of applying DTIA to different case studies and the interpretations of the extracted insights and their projections on the physical domain of knowledge.
- Chapter Four: This chapter includes the conclusion of the presented work and an outlook for what can be performed in future work.

1.1.1 Study I

In this study, we propose the use of a decision tree classifier (DTC) to differentiate between severe accident scenarios and extract physical insights from their distinctive features. The DTC model provides numerical thresholds for each feature, enabling classification. Upon further analysis, these thresholds can highlight critical insights that are often overlooked in conventional studies. The dataset used to train the model was generated with MELCOR, an integral severe accident code. Two primary scenarios were simulated: SBO and a large-break LOCA (0.1 m^2 break at the main steam line) with SBO, each with and without the IVR strategy, resulting in four cases. The simulations modelled a Nordic BWR with a nominal thermal power of 3000 MWth, where the thermal-hydraulic response was calculated as a function of time, including vessel surface temperatures, pressures, and internal conditions. The MELCOR mesh divides the lower plenum into 28 uneven segments, from which the maximum external temperature at each time step was selected to construct a sub-dataset of two features, Time and Temp. In total, the training dataset consisted of 1084 samples [80].

1.1.2 Study II

In this study, we employed the decision tree classification (DTC) algorithm as a tool for exploratory data analysis, rather than as a conventional predictive model for classifying outcomes based on input features. While the development of a robust DTC model is an inherent by-product of the approach, it is not the primary objective of this work. Instead, the focus is on demonstrating how our automated systematic framework, the Decision Tree Insight Analysis (DTIA) tool, can uncover meaningful regions within the input feature space that provide deeper insights into the underlying phenomena. To evaluate the method, we applied it to both synthetic and experimental datasets across several domains, including nuclear reactor safety, single-cell RNA sequencing in mice for neurodegenerative disease studies, and RNA sequencing for breast cancer staging in humans. The article is mostly covered in the methods section. The methods section introduces the developed approach, outlining its theoretical foundations, assumptions, expected outcomes, and limitations. The results and discussion (included in the methods sections as well) then present the outcomes of applying the method to different fields of research. This is followed by a comparison between the proposed DTIA framework and other techniques, such as the feature importance attribute in random forests and feature ranking through K-means clustering [81].

1.1.3 Study III

In this study, we applied the Decision Tree Insights Analytics (DTIA) framework. Specifically, we examined the COR package results generated by MELCOR for a station blackout (SBO) combined with a loss-of-coolant accident (LOCA) in a Nordic boiling water reactor (BWR). This particular accident scenario has previously been analysed in the work of Chen et al., and in this study, we utilised the same dataset. The extracted COR package output comprised 23,950 parameters, which were processed through DTIA to determine those most influential in distinguishing the timing of the key events originally identified by Chen et al. The critical events considered in this analysis were the failure of the core support plate at 6183 seconds, containment venting at 11,131 seconds, and failure of the reactor pressure vessel lower head at 24,863 seconds. Accordingly, the problem was formulated as a classification task in which time intervals were assigned discrete labels: 0 for 0–6183 seconds, 1 for 6183–11,131 seconds, 2 for 11,131–24,863 seconds, and 3 for 24,863–90,000 seconds (the end of the simulation). The input features corresponded to the temporal behaviour of the COR package parameters. The MELCOR model was defined with 21 radial rings and 60 axial levels, and the parameters used in the DTIA analysis are summarised in Table 1. Each parameter contained 772 time points, with each time point treated as an individual sample, resulting in an input matrix of 772 rows by 23,950 columns [82].

1.1.4 Study IV

In this study, we applied DTIA to structural analysis parameters resulting from ANSYS calculations to the reactor pressure vessel's lower head due to loads from two different severe accidents, SBO and SBO + LOCA. The purpose of this work was to find the similarities and differences between the two cases at the time of failure. Since we are studying the structural state at the time of failure for the two cases, differences in 2D plots were almost non-conclusive for comparative studies. However, each accident has been analysed in a previous study by Hongdi Wang et al. Hence, the data we used were the nodal solution results from ANSYS calculations in the two cases. DTIA managed to reveal some of the overlooked insights that provide preliminary information on the mode of failure in different accidents.

1.1.5 Study V

In this study, we present a modified framework that couples K-Means Clustering with DTIA to perform an in-depth analysis of the time-dependent progression of severe accidents in Nordic boiling water reactors (BWRs). Specifically, K-means clustering was employed to identify timestamps linked to different phenomenological behaviours in the COR package results obtained from MELCOR simulations. The underlying rationale is that if a phenomenon occurs within a specific time interval, the corresponding time points will naturally group into the same cluster. The purpose of developing such a framework is to allow the time-series data to reveal its own structure, indicating regions of interest in a high-dimensional dataset. This approach reduces the dependence on expert subjectivity during the initial stages of analysis, while still relying on expert knowledge to interpret the physical meaning of the extracted insights.

The case study investigated in this work is the time-wise progression of a station blackout (SBO) occurring simultaneously with a loss-of-coolant accident (LOCA) in the Nordic BWR. This combined event sequence has previously been simulated using MELCOR and extensively analysed by Chen et al., who identified three critical timestamps corresponding to major accident phenomena: 6183 seconds for core support plate failure, 11131 seconds for containment venting, and 24863 seconds for reactor pressure vessel lower head failure. The framework proposed here builds on this foundation by applying K-means clustering to the same MELCOR COR package dataset, enabling the identification of relevant timestamps directly from the data. The choice of K-means over other temporal clustering approaches stems from its distance-based structure, which offers higher explainability when integrated with downstream interpretable models.

Following clustering, the assigned labels are analysed using the Decision Tree Insights Analytics (DTIA) method to identify the most influential parameters among the 23,950 considered in the COR package, as summarised in Table 1. The MELCOR COR model of Chen et al. divides the reactor core into 21 radial rings and 60 axial levels, with accident progression simulated over a total duration of 90,000 seconds, discretised into 722 time points. Consequently, the input matrix used for K-means clustering, and subsequently for DTIA analysis, consisted of 722 rows and 23,950 columns.

Table 1. Breakdown of the Considered Parameters for DTIA Time-Wise Analysis for SBO + LOCA Accident Progression in Nordic BWR (Taken from Paper 3)

Type	MELCOR Code	Parameter	Number of Rings	Number of Axial Levels	Total Number of Cells
Mass	MUO2	Uranium Oxide	21	60	1260
	MZR	Zirconium	21	60	1260
	MZRO2	Zirconium Oxide	21	60	1260
	MSS	Support Structure	21	60	1260
	MSSOX	Support Structure Oxide	21	60	1260
Particulate Debris Mass	PD_MUO2	Uranium Oxide	21	60	1260
	PD_MZr	Zirconium	21	60	1260
	PD_ZrO2	Zirconium Oxide	21	60	1260
	PD_SS	Support Structure	21	60	1260
	PD_SSOX	Support Structure Oxide	21	60	1260
Particulate Debris Mass in the Bypass	PB_UO2	Uranium Oxide	21	60	1260
	PB_ZR	Zirconium	21	60	1260
	PB_ZRO2	Zirconium Oxide	21	60	1260
	PB_SS	Support Structure	21	60	1260
	PB_SSOX	Support Structure Oxide	21	60	1260
Temperatures	TSVC	Channel Fluid	21	60	1260
	TFU	Fuel	21	60	1260
	TCL	Clad	21	60	1260
	TSS	Support Structure	21	60	1260
Hydrogen Production	DMH2_TOT	Total	-	-	-
	DMH2_ZIRC	Zircalloy	-	-	-
	DMH2_SS	Support Structure	-	-	-
	DMH2_B4C	B4C	-	-	-
Totals	EFPD_TOT	Fission and Decay heat energy	-	-	-
	EMWR_TOT	Oxidation Heat Generation	-	-	-
	EB4C_TOT	B4C Interactions Heat Generation	-	-	-
Rates	EFPD_RAT	Fission and Decay heat energy	-	-	-
	EMWR_RAT	Oxidation Heat Generation	-	-	-
	EB4C_RAT	B4C Interactions Heat Generation	-	-	-
Total Number of Parameters					
23950					

2 Decision Tree Insights Analytics (DTIA) Evolution

Decision tree insights analytics (DTIA) is a generic framework. It uses the decision tree classification (DTC) algorithm's high interpretability and explainability to identify domains of interest associated with categorical outputs from high-dimensional data records. DTIA focuses on finding the patterns between inputs and categorical outputs. Having well-developed and optimised classifiers is a byproduct. However, it is not the primary objective behind the utilisation of DTIA. This chapter explains the journey of DTIA development, starting from the theoretical background of the DTC, followed by the description and utilisation of the DTIA framework. An overview of the K-Means clustering and finally, the development of the K-means guided DTIA framework.

2.1 Overview of the Decision Tree Classification Algorithm

Supervised machine learning (SML) is defined as a process where the data used to develop the model includes both input features and their corresponding outputs. The developed SML models try to learn the patterns between inputs and outputs. It can be divided into two categories: 1) regression problems and 2) classification problems. In Regression problems, input features and target outputs are numerical values. In Classification problems, input features are numerical values, while target outputs are categorical (classes). During the SML model development, it passes through at least two necessary stages: 1) model training and 2) model validation and testing. In model training, the algorithm minimises the error between the desired outcome (the true output from the original data) and the predicted outcome (the model’s output). In the model validation and testing, we test the final model on unseen data to evaluate its performance and measure its error compared to the ground truth values.

Decision tree classification (DTC) is one of the most robust techniques in supervised machine learning (SML). It is also highly interpretable and explainable, making it easier to understand how and why the developed model performed in a certain way. In DTC, the algorithm poses a series of true or false questions, splitting the data into two or more categories based on the input features, depending on the problem. A typical DTC consists of nodes and leaves. A node is when a question is asked, and a leaf is when no more questions are asked. The objective of the series of questions the DTC asks is to reach pure leaves where each leaf has a single category rather than mixed categories, as illustrated in Figure 1. That said, DTC can easily overfit due to its conversion into an exhaustive search, rather than identifying patterns between inputs and outputs.

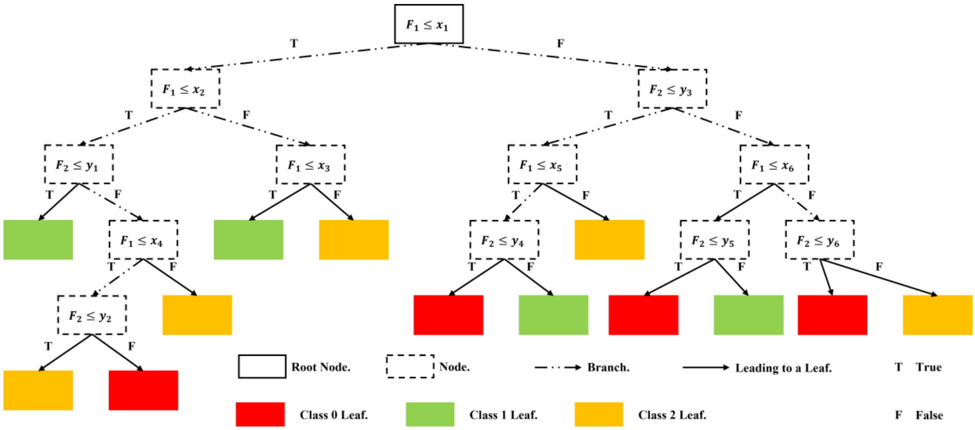

Figure 1. Decision Tree Classification Schematic for Three-Class Output (Taken from Paper 1 [80])

2.1.1 Decision Tree Classification: Theoretical Background

The theoretical background of DTC is based on evaluating how good a question is. This evaluation is statistically evaluated through the calculation of the information gain from asking a specific question. Information gain is built on the basis of information theory. Information theory in its modern form is defined as the study of quantifying information in general. In the scope of DTC studies, information gain can be considered equivalent to reducing the uncertainties associated with the data. Classification data uncertainty can be quantified and represented via the dataset's entropy or impurity. Two major types of data uncertainties are considered in DTC: 1) Gini impurity and 2) entropy. Gini impurity represents the probability of misclassifying a data point in a given pool, and it is calculated using Equation 1. Entropy, on the other hand, is calculated using Equation 2, and it represents the mean amount of information transferred from a random trial. That being said, entropy and Gini impurity seem similar. However, the two have some differences; the main difference is the Gini impurity's linearity measure compared to the entropy's logarithmic measure. This difference makes Gini impurity more sensitive, more computationally efficient and interpretable as the mean error of a developed classifier. On the other hand, Entropy is more robust and interpreted as the quantified information needed to classify a specific category correctly. That being said, information gain can be considered as the reduction in Gini impurity or entropy caused by applying a certain rule or asking a specific question. Information gain can be calculated using Equations 3 and 4 for Gini impurity and entropy, respectively.

$$G_I = 1 - \sum_{i=1}^{k} p_i^2 , \qquad (1)$$

$$Entropy\ (E) = - \sum_{i=1}^{k} p_i log_2(p_i) , \qquad (2)$$

$$IG = G_{I_P} - \left[\left(\frac{N_{left}}{N} * G_{I_{left}} \right) + \left(\frac{N_{right}}{N} * G_{I_{right}} \right) \right], \qquad (3)$$

$$IG = E_P - \left[\left(\frac{N_{left}}{N} * E_{left} \right) + \left(\frac{N_{right}}{N} * E_{right} \right) \right], \qquad (4)$$

where G_I is the Gini impurity, E is the entropy, IG is the information gain, k is the number of categories (classes), p_i is the probability of finding a data point that belongs to a class i in the data pool, G_{I_P} is the Gini impurity in the parent node (before applying the suggested rule), E_P is the Entropy in the parent node, N is the total number of samples, $left$ is the left branch (conventionally True) after applying the rule suggested in the parent node, $right$ is the right branch emerging from the parent node (conventionally False).

2.1.2 Decision Tree Classification Implementation

The decision tree classification algorithm is built top to bottom, starting from the root node until the leaves. Training data is fed to the root node, where the first split has to be decided. Deciding the split has two dimensions. 1) choosing the input feature upon which the data will be split, and 2) calculating the threshold that will be used to create the splitting rule. First, for each input feature, the values are sorted. Then, the potential split thresholds are calculated by finding the midpoint between each two successive points using Equation 5, where $F_{i_{s_j}}$ is the value for the sample number j in feature number i. Then, each of these potential thresholds is tested to evaluate the reduction in Gini impurity or entropy (information gain). After evaluating all the information gain values from all potential thresholds across all features, the potential threshold for a particular feature that provides the highest information gain is selected as the root node. That said, the DTC algorithm tries to maximise the information gain as it is built from top to bottom. Hence, it is a greedy algorithm in that sense. This process of evaluating features' potential thresholds and choosing the split rule that would maximise the information gain is repeated for every required split until there are only pure leaves or the algorithm reaches a stopping criterion. DTC's dependency on greediness doesn't always yield the optimal solution as a classifier. It also makes DTC prone to overfitting because the stepwise approach of searching for the splitting rules can tend towards an exhaustive search algorithm.

$$potential\ threhsolds = \frac{F_{i_{s_j}} + F_{i_{s_{j+1}}}}{2}, \qquad (5)$$

Early stopping criteria can be deployed to prevent the DTC from converting to an exhaustive search algorithm. Two main hyperparameters in the DTC algorithm can be deployed to act as early stopping criteria. 1) minimum number of samples per leaf and 2) maximum depth of the developed tree. Specifying the minimum number of samples per leaf prevents the algorithm from performing extra splitting when any potential split would result in fewer samples than the prespecified minimum. The maximum depth of the tree stops the algorithm from performing extra splits when the prespecified maximum depth is reached. While the aforementioned hyperparameters do not improve the issues associated with the greediness of the DTC algorithm, they prevent the algorithm from choosing splitting rules for each sample. A summary of the DTC algorithm flow chart is illustrated in Figure 2.

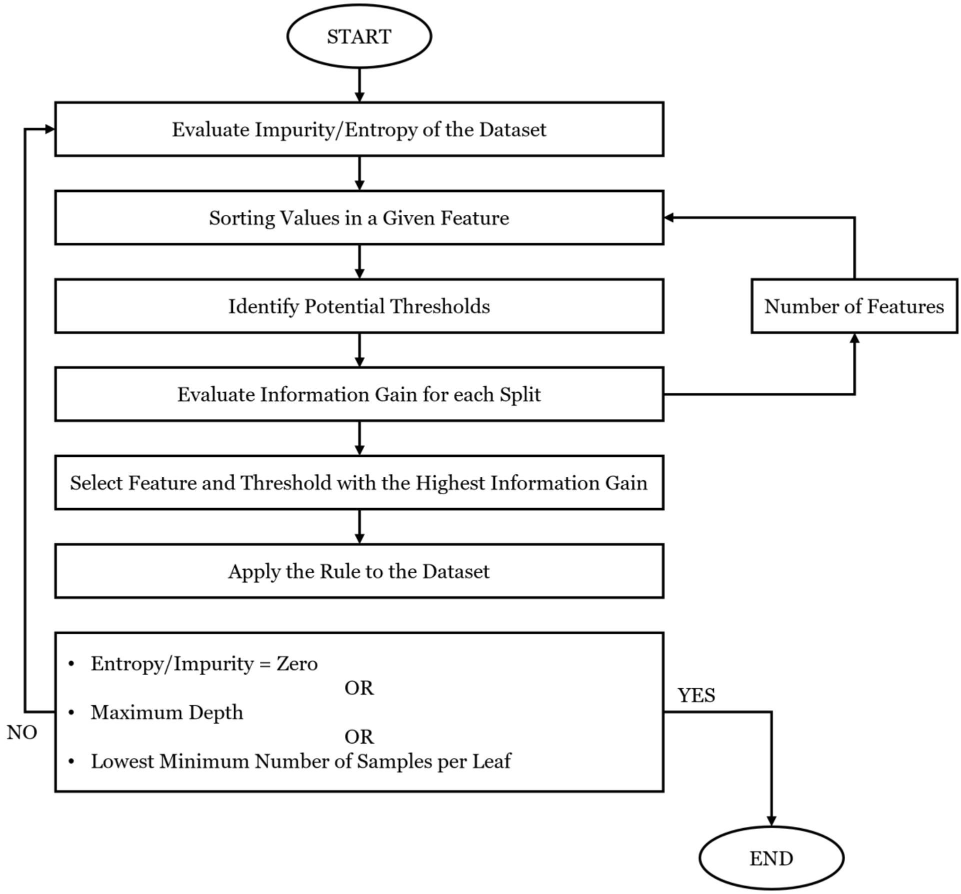

Figure 2. Flow Chart of the Decision Tree Classification Algorithm.

2.1.3 Decision Tree Classification Application and Practical Aspects

Some ready-to-use libraries employ the DTC algorithm directly on the input data. As mentioned earlier, to build a DTC model capable of predicting categories from numerical input (input features), the model has to be trained on some of the data and then tested on the rest of the dataset. The training aims to find the best splitting rules to classify the data correctly. The test process tests the developed model's performance on unseen data. That being said, DTC is an SML algorithm. SMLs are known for their ability to interpolate between data points; extrapolation is not their strongest suit. Several metrics can be used to evaluate an SML model's performance. We used four metrics for classification:

1) accuracy, 2) precision, 3) recall and 4) F1-score using Equations 6, 7, 8 and 9, respectively.

$$Accuracy = \frac{TPC + TNC}{TPC + TNC + FPC + FNC}, \qquad (6)$$

$$Precision = \sum_{i}^{n} w_i \frac{TPC}{TPC + FPC}, \qquad (7)$$

$$Recall = \sum_{i}^{n} w_i \frac{TPC}{TPC + FNC}, \qquad (8)$$

$$F_1\ Score = \sum_{i}^{n} w_i \frac{2(Recall * Precision)}{Recall + Precision}, \qquad (9)$$

Assuming a binary classification problem, the two classes can be referred to as positive and negative. In that notation, TPC (true positive class) and TNC (true negative class) refer to the number of samples correctly predicted as positive and negative classes, respectively. On the other hand, FPC (false positive class) and FNC (false negative class) refer to the number of samples mispredicted as positive while they are negative samples and the samples mispredicted as negative while they are positive, respectively. It is worth mentioning that accuracy (calculated using Equation 6) is a global performance metric and can be misleading in the case of data imbalance. Data imbalance occurs when the number of samples per category (class) is not equal. Precision, recall and F1-score can handle data imbalance as they are weighted, where the w_i in Equations 7, 8 and 9, the weight of the class i in the data set (number of samples belonging to each class divided by the total number of samples) and n is the total number of classes in the dataset.

The ultimate purpose of developing any SML is to generalise over the training data. Generalisation in that context refers to learning the patterns between inputs and outputs. In classification problems, generalisation is achieved when the developed model can learn the patterns between the numerical input features and the categorical (classes) outputs. The performance of any SML classifier can be categorised into three main categories: 1) underfitting, 2) overfitting and 3) perfect fit. Underfitting is when the developed model performs poorly during training and testing. This means the model with its hyperparameters couldn't find the patterns between the inputs and outputs. Overfitting occurs when a developed model performs well during training but poorly during testing. In other words, the developed model memorised the training data. No patterns were found that could be applied to another dataset within the same domain as the training dataset. Finally, the perfect or near-perfect fit is when the model performs well during training and testing. It indicates the developed model's ability to learn patterns between input features and their associated classes, and to apply these patterns successfully to another dataset during the testing process. For classification problems, the aforementioned training and testing performances are measured using the metrics described in Equations 6, 7, 8 and 9.

Cross-validation is essential to ensure the developed model's generalisation capability. Sometimes, a developed model can show a perfect fit performance while training and testing on a certain dataset split. In this case, the patterns learned by the model from the training dataset samples are directly applicable to the test dataset samples. This is sometimes referred to as the developed SML 'getting lucky'. To achieve more robustness and trust in the model's generalisation capabilities, cross-validation is used, where the model is retrained and tested several times (folds), and the mean performance metrics are reported. The number of samples is the same for each training and test fold. However, the samples are changed, meaning that some of the samples in the training are included in the test and vice versa. That being said, there are two main approaches to perform cross-validation: 1) the leave-one-out method, and 2) the random selection method. In the leave-one-out method, assuming a typical training/test dataset split of 80% training and 20% test, the samples selected in the test dataset rotate, replacing the training dataset. In that case, five folds are needed to ensure that all the samples have been included in the test dataset. The random selection method uses another approach where the samples included in the training and test datasets are randomly chosen every time the model is retrained. The output of this method shows how different the division of samples between training and test impacts the model's performance.

2.1.4 Insights Extraction from Decision Tree Classification Interpretability and Explainability

The decision tree classification (DTC) algorithm is a self-explanatory SML model because it uses a step-wise approach to searching for splitting rules while building the tree. That said, information gain upon which the tree was built during training can lead to insights extraction associated with the modelled problem. Two common approaches are used for insights extraction: 1) calculating the feature importance, and 2) gathering the information at each node in the developed tree. Feature importance refers to a weighted ranking system (ranging from zero to one) of the input features and their associated importance in correctly classifying the target classes. The higher the value, the more important the feature is in solving the problem. The second approach, gathering information at each node, is more fluid than the feature importance calculation approach. It is more detailed in observing the details of each rule (feature and associated threshold) used in each node and its impact on the classification process. The rules extraction process gives more information about the domain combinations to which most of each class belongs. The two aforementioned approaches will then be projected onto the physical domain of knowledge to better understand the relationship between input features and the target classes. In summary, feature importance can be considered a global numerical metric measuring the association between inputs and outputs. On the other hand, the rules extraction approach uses the rules combinations to find different classes.

Although extracting insights from DTC modelling is easy, measuring their robustness is crucial. The classification metrics mentioned above can measure the robustness of insights. Hence, the necessary step is to ensure that the model generalisation and robustness directly impact the quality of the extracted information. We developed a step-wise approach consisting of five sequential steps that ensure the developed model's hyperparameter tuning, leading to robust generalisation capabilities, as shown in Figure 3. First, testing the DTC algorithm's capability to map the input features to the associated target classes. We train a DTC with default hyperparameters on the problem's data, report training, and test accuracy metrics. Second, the hyperparameter tuning process involves developing a number of DTCs varying in the minimum number of samples per leaf and the maximum depth of the tree. Third, to eliminate overfitting models, we select the models with a difference between test and training precision less than a specific threshold (it varies based on the problem nature and the domain). Fourth, eliminating the under-fitting models by excluding the models with average test metrics less than a prespecified threshold based on the problem nature and its associated domain. Finally, all the models that passed steps three and four are retrained via a random cross-validation approach. We select the final model that provides the test performance metrics' highest mean and lowest associated standard deviation. This final step ensures that none of the selected models got lucky during the previous selection process, giving statistical confidence about the chosen model metrics.

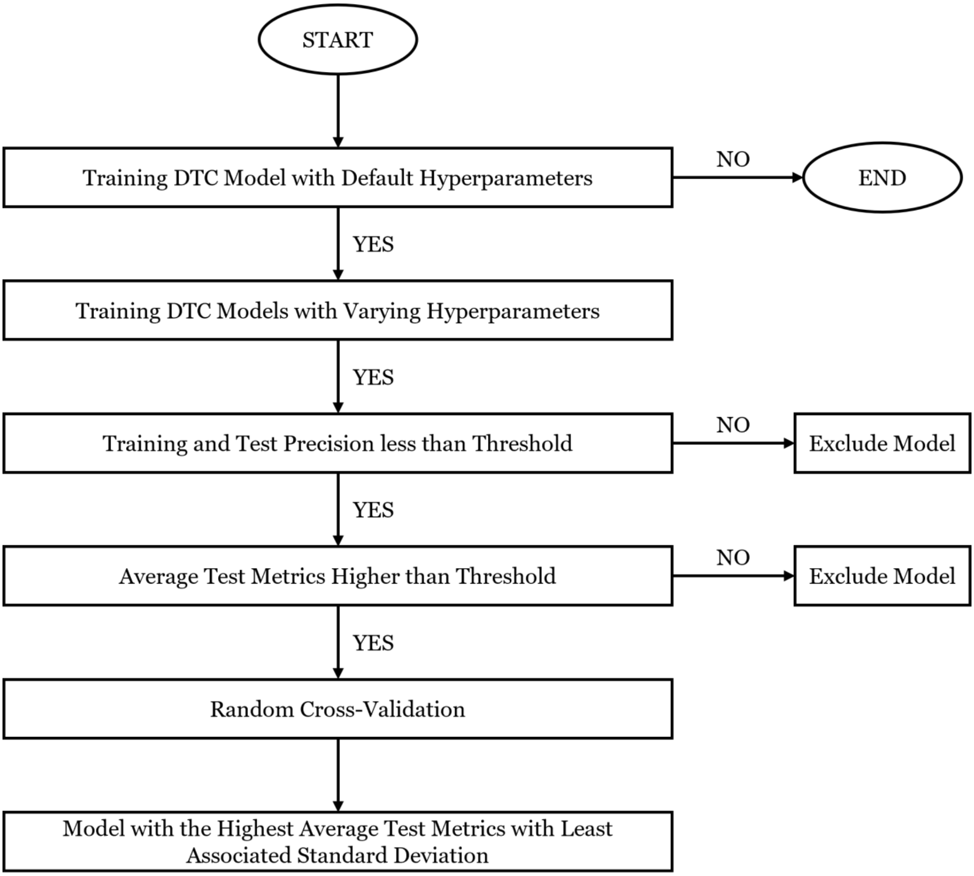

Figure 3. Decision Tree Classifier Hyperparameters Tuning Process.

We applied the step-wise approach to a time-dependent severe accident scenario in a Nordic boiling water reactor (BWR), aiming to distinguish between four accident cases using just two input features: (1) time and (2) the maximum external surface temperature of the reactor pressure vessel (RPV). The scenarios included: 0) SBO without IVR-ERVC, 1) LOCA + SBO without IVR-ERVC, 2) SBO with IVR-ERVC, and 3) LOCA + SBO with IVR-ERVC. In the decision tree classification (DTC) framework, this corresponds to two features and four class labels. Each time step was treated as a separate sample, resulting in a total of 706 samples. Figure 4 presents the temporal evolution of the RPV's external maximum temperature. Visually, notable differences are observable between scenarios 0 and 1, and 2 and 3 after 5,000 seconds. However, before 5,000 seconds, distinguishing between the four cases lacks statistical reliability. Similarly, differentiating between scenarios 2 and 3 becomes challenging beyond 10,000 seconds.

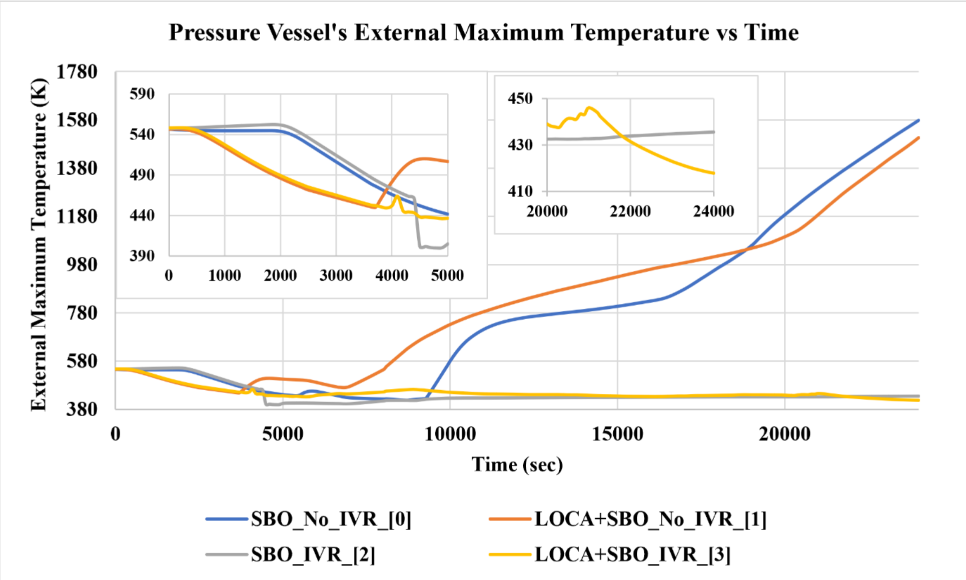

Figure 4. Time-Wise Maximum External Temperature of the Reactor Pressure Vessel. (Taken from Paper 1 [80])

The developed classifier employed a Decision Tree Classifier (DTC) with a minimum of 22 samples per leaf. To evaluate its performance, we conducted random cross-validation and reported the mean and standard deviation for each classification metric. Additionally, we incorporated a relative error metric, calculated using Equation 10 and summarised in Table 2, to assess the classifier's robustness. Given the multiclass nature of the task (four accident categories), a detailed class-wise evaluation was necessary to ensure reliable insights, as shown in Table 3. Figure 5 presents the confusion matrix, providing a visual summary of correct predictions versus misclassifications and highlighting how the model incorrectly classified one accident scenario as another.

$$Relative\ Error = \frac{Standard\ Deviation}{Mean}, \qquad (10)$$

We analysed the structure of the trained decision tree used to classify the accident scenarios, as illustrated in Figure 6. Each node or leaf shows the number of data points it contains ("Samples"), while the "Class" set indicates how those samples are distributed across classes 0, 1, 2, and 3. We explored all possible decision paths in the tree, each defined by a sequence of feature-based threshold rules. Although Figure 6 shows eight distinct paths, we evaluated their effectiveness by applying these rule combinations across the entire dataset, with results listed in Table 4. Among them, paths P1, P2, P4, P6, and P7 achieved the highest training and test accuracies. To reflect their significance, we computed weighted path accuracies based on the sample counts in both training and testing sets, as presented in Table 5.

Table 2. Cross-Validated Developed Performance. (Taken from Paper 1 [80])

	Training Accuracy	**Training Precision**	**Training F1 Score**	**Training Recall**	**Test Accuracy**	**Test Precision**	**Test F1 Score**	**Test Recall**
Mean	0.86	0.86	0.86	0.86	0.82	0.81	0.81	0.81
Standard Deviation	0.01	0.01	0.01	0.01	0.03	0.03	0.03	0.03
Relative Error	0.01	0.01	0.01	0.01	0.03	0.03	0.03	0.03

Table 3. Selected Model Class-Wise Performance. (Taken from Paper 1 [80])

<table>
<tr><th></th><th>Training Accuracy</th><th>Training Precision</th><th>Training F1 Score</th><th>Training Recall</th><th>Test Accuracy</th><th>Test Precision</th><th>Test F1 Score</th><th>Test Recall</th></tr>
<tr><td>Class 0</td><td rowspan="5">0.87</td><td>0.78</td><td>0.81</td><td>0.85</td><td rowspan="5">0.79</td><td>0.71</td><td>0.75</td><td>0.79</td></tr>
<tr><td>Class 1</td><td>0.89</td><td>0.80</td><td>0.73</td><td>0.76</td><td>0.66</td><td>0.59</td></tr>
<tr><td>Class 2</td><td>0.91</td><td>0.94</td><td>0.97</td><td>0.84</td><td>0.89</td><td>0.94</td></tr>
<tr><td>Class 3</td><td>0.9</td><td>0.91</td><td>0.92</td><td>0.88</td><td>0.86</td><td>0.84</td></tr>
<tr><td>Mean</td><td>0.87</td><td>0.87</td><td>0.87</td><td>0.8</td><td>0.79</td><td>0.79</td></tr>
</table>

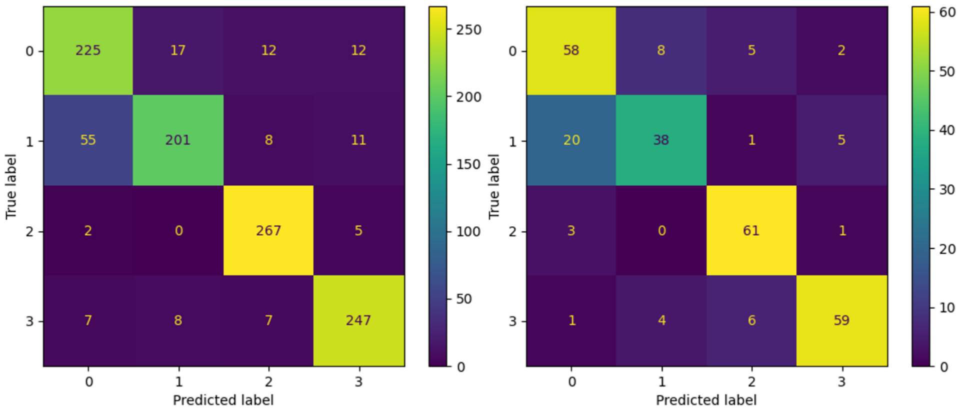

A: Training Confusion Matrix **B: Test Confusion Matrix**

Figure 5. Developed Classifier Training and Test Performance Confusion Matrices. (Taken from Paper 1 80)

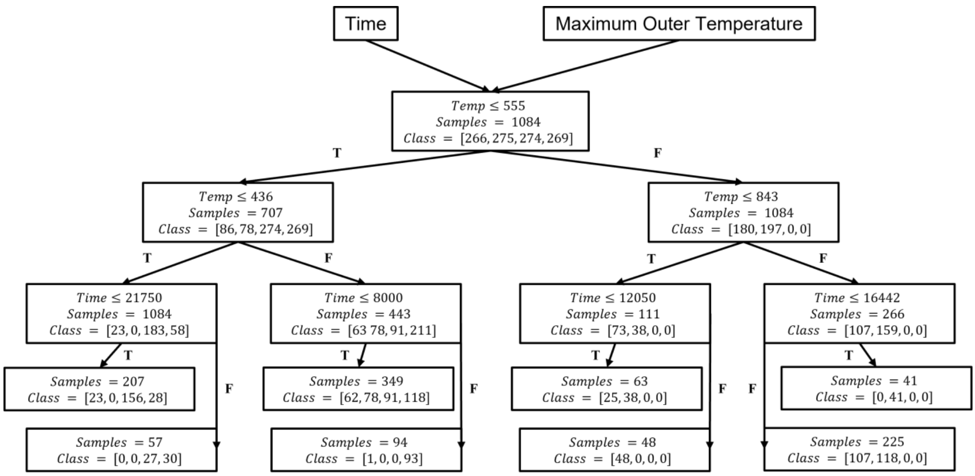

Figure 6. Decision Paths (Up to Depth Three) for the Selected Decision Tree Model. (Taken from Paper 1 80)

Table 4. DT Paths Training and Test Accuracies (Taken from Paper 1 [80])

Label	Threshold	Training Accuracy	Test Accuracy
P1	$Temp \leq 436$ $Time \leq 21750$	0.95	0.96
P2	$Temp \leq 436$ $Time > 21750$	0.98	0.94
P3	$436 < Temp \leq 555$ $Time \leq 8000$	0.8	0.68
P4	$436 < Temp \leq 555$ $Time > 8000$	0.99	1
P5	$555 < Temp \leq 843$ $Time \leq 12050$	0.67	0.5
P6	$555 < Temp \leq 843$ $Time > 12050$	1	1
P7	$Temp > 843$ $Time \leq 16442$	1	1
P8	$Temp > 843$ $Time > 16442$	0.82	0.7

Table 5. Weighted Paths Accuracies (Taken from Paper 1 [80])

Label	P1	P2	P3	P4	P5	P6	P7	P8
Weighted Path Accuracy	0.95	0.97	0.78	0.99	0.64	1	1	0.8

We applied the rule sets from each of the identified paths to the full dataset, resulting in the division of Figure 4 into five subfigures, presented in Figure 7. While the thresholds in P1 did not yield strong distinctions between accident types, they offered a valuable negative insight: within the time and RPV surface temperature range defined by P1, the LOCA + SBO scenario without IVR could not occur. This makes P1 helpful in inferring the absence or presence of IVR in such cases. In the P2 subfigure, both accidents meeting P2's thresholds shared the presence of IVR, though the insight arrives too late, after significant core damage. Interestingly, another accident type also met the thresholds defined by P4, highlighting the need for expert validation and refinement of the DT-derived rules. Subfigures P6 and P7 revealed that the dominant accident types were SBO and LOCA + SBO, both of which lacked IVR activation. Overall, the insights from the decision tree model offer a valuable foundation for causality analysis, enabling a deeper understanding of accident progression mechanisms. This knowledge can ultimately inform the design of improved safety systems, operational protocols, and accident mitigation strategies.

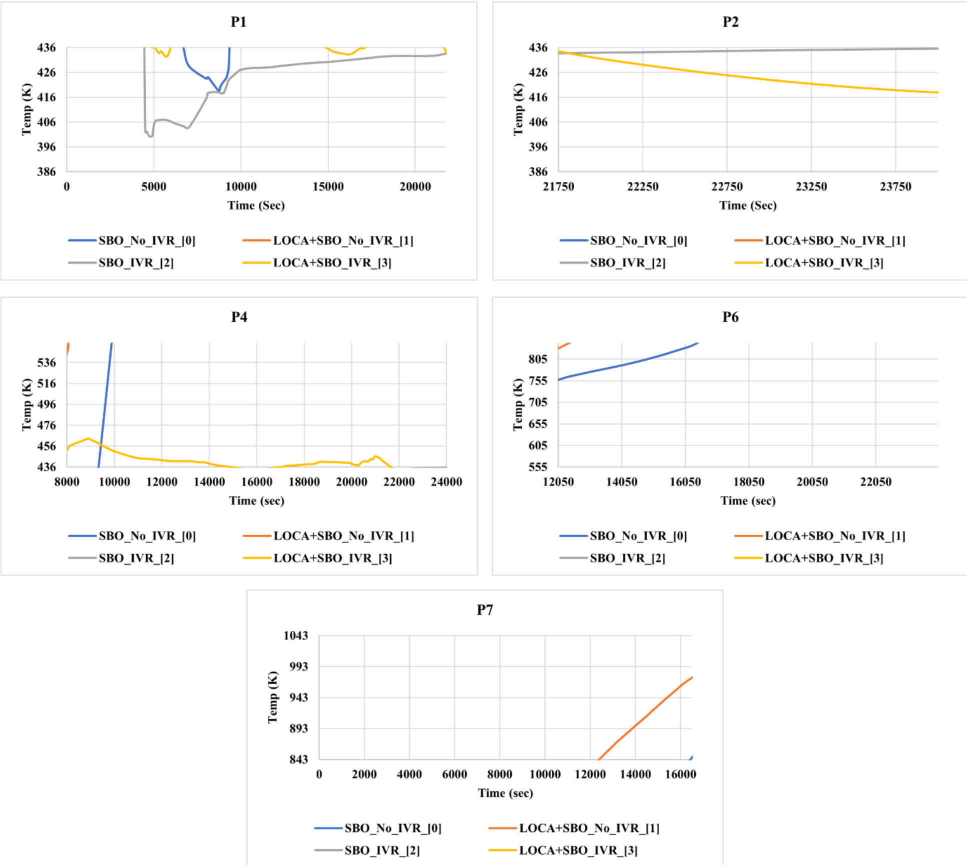

Figure 7. Application of the Extracted Paths on the Reactor Pressure Vessel's Time-Wise External Wall Maximum Temperature for Different Accident Scenarios. (Taken from Paper 1 [80])

2.2 Decision Tree Insights Analytics (DTIA) Framework

Decision tree insights analytics (DTIA) is a generic analytical framework built on decision tree classification (DTC). Hence, it can be applied to different datasets across different fields of study. DTIA extracts the combination of input features domains that lead to target classes. The main assumption and limitation of DTIA is that DTC can map the input features to the target classes with a particular range of classification metrics. This section will cover the theory of operation of DTIA, as well as the differences between DTIA and Random Forest (RF) feature importance attributes, and the generic applications and use cases of DTIA. The DTIA package can be found open access on github via the link (https://github.com/KHossny/DTIA)

2.2.1 DTIA Methodology

The DTIA method consists primarily of five sequential steps as shown in Figure 8. First, developing decision tree classifiers with varying hyperparameters. Second, selecting the top performing models from a classification metrics point of view. Third, finding the typical decision tree structure for all the selected models. Fourth, extracting the features and their associated thresholds used at each node after adjusting all the developed trees to the typical structure. Finally, post-process the insights gathered from step four.

In step one, data is split into training and test sets and fed to the DTC algorithm with varying hyperparameters (minimum number of samples per leaf and maximum depth of the developed tree), with the number of folds for random cross-validation prespecified. BY the end of step one, a large number of decision tree classifiers would have been developed to map the input features to the output classes. However, not all the developed models had a good classification performance. Hence, insights extracted from poorly performing models wouldn't be trustworthy, as these models were not capable of mapping inputs to the output classes. That is when step two comes into play to filter out the poorly performing models.

In Step two, all the developed DTCs pass two selection criteria. First, the difference between the developed DTC's performance over training and test data from a precision point of view. Second, the developed DTC's average classification performance over the test dataset. By the end of step two, there will be a number of developed DTCs that are well-performing over both training and test datasets. That said, the selected models will be used for insights extraction. However, not all of these models have the same decision tree structure. Hence, it will be challenging to derive global statistical insights from all the developed models. That is the purpose of step three, which is finding the typical DTC structure.

In step three, DTIA collects all the depths of the models that passed the selection criteria in step two. The DTC structure with the least depth is then selected as the typical DTC structure upon which all global statistical insights will be gathered. The rationale behind choosing the structure with the least depth is based on the number of rules required to achieve the same range of classification metrics. The lower the number of rules needed, the higher the information gain from each rule (feature used and its associated threshold). Figure 9 shows four different abstract DTC structures that achieve the same classification performance. The second tree from the left is the shortest one. Hence, all the other developed trees will be cut at depth two to mimic the depth of the shortest tree. Having a quasi-similar tree structure facilitates the process of extracting global statistical insights from all the developed trees in step four.

In step four, DTIA summarises the used features (input dimensions) and their associated thresholds for each node in the typical DTC structure. The colour code for circular nodes in Figure 9 denotes a similar position of the node in each of the trees. Having such a summary helps with gaining broad insights about the modelled problem. For example, assuming 100 models passed the selection criteria, feature x appeared in the root node in 90 of the models. Given the theoretical background of decision trees, we can conclude with 90% confidence that feature x is the most influential feature (providing the maximum information gain) in splitting the different classes in this problem. Following up on the same example, the associated thresholds can reveal more in-depth information, such as the boundaries (set points) and their impact on separating the different classes.

Finally, DTIA provides extensive information about the modelled problem, including details about each of the developed DTCs that passed the selection criteria, along with their hyperparameters. This introduces flexibility in the post-processing of DTIA insights, allowing them to be projected into the domain of knowledge more effectively. That being said, although having a well-developed DTC model is not the primary objective of DTIA. DTIA saves the developed DTCs that can be used later for their predictive modelling capabilities.

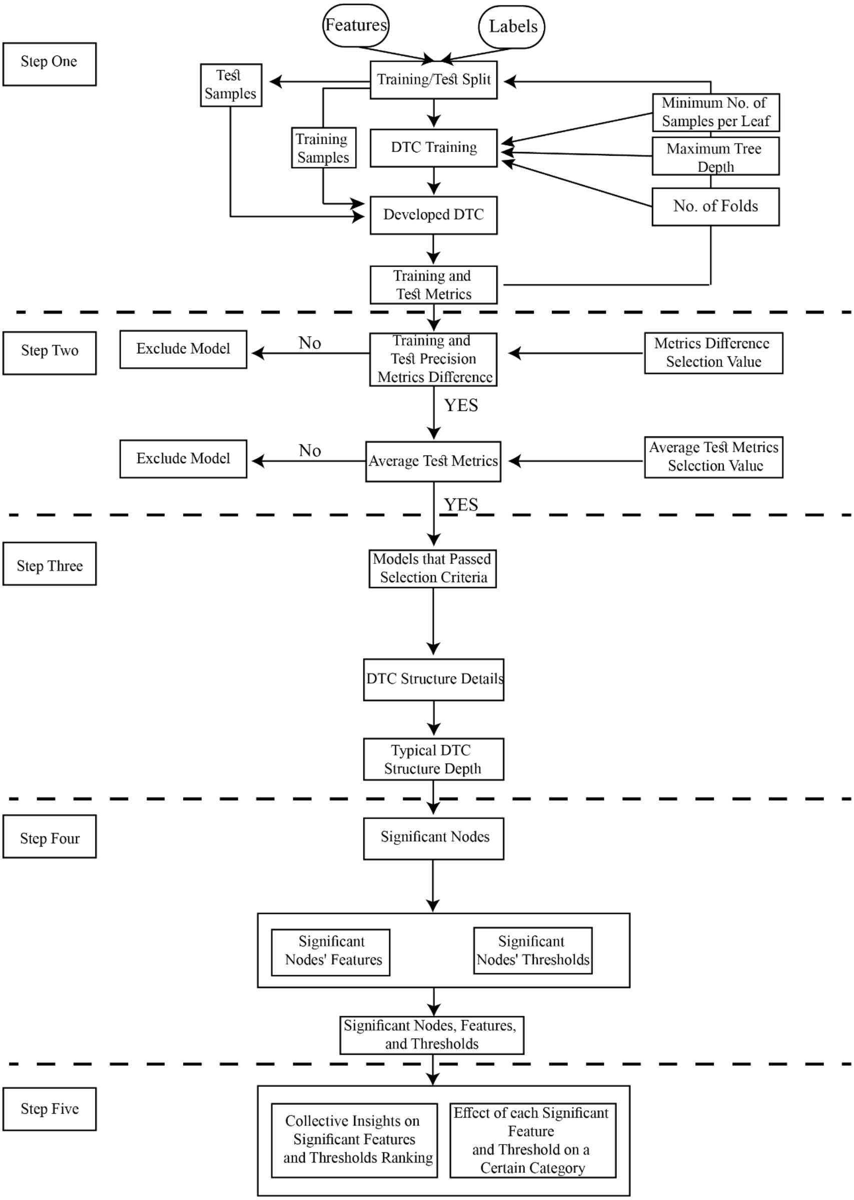

Figure 8. Decision Tree Insights Analytics (DTIA) Framework Flow Chart. (Taken from Paper 2 [81])

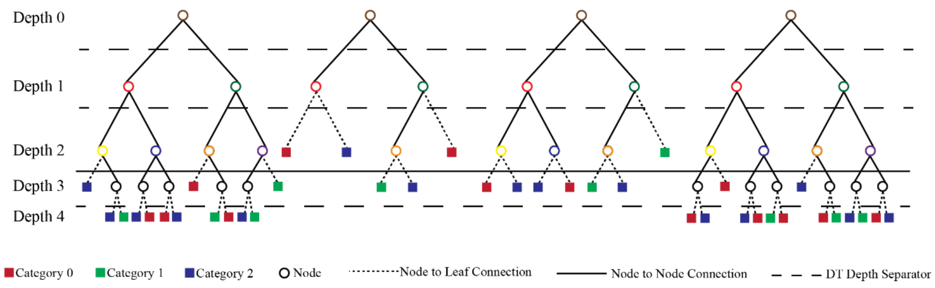

Figure 9. Step Three: Choosing the Typical Decision Tree Classifier Structure. (Taken from Paper 2 [81])

2.3 DTIA Applications across Fields of Science

We applied DTIA across three distinct research problems spanning both physical and biological sciences. The first case study, from the physical sciences, focused on analysing hydrogen generation and radioactive mass release during two severe accident scenarios. The second and third case studies were rooted in biology. In Case Study II, we aimed to uncover strong associations between single-cell RNA sequencing data and Niemann-Pick disease type C1 (NPC) in mice. In the more complex Case Study III, we attempted to link RNA sequencing data with breast cancer staging in humans. While the method yielded valuable insights in the first two cases, its effectiveness was limited in the third, likely due to numerical input variability, sampling biases tied to tumour heterogeneity, and the subjective nature of the cancer staging labels. In Case Study I, we will demonstrate how DTIA contributed to the formulation of a research question. In contrast, Case Study II will highlight novel insights uncovered by DTIA that merit further validation by domain experts.

2.3.1 Case Study I: DTIA Application to Hydrogen Production and Radioactive Mass Release During Nuclear Reactor Severe Accident Progression

In nuclear reactor safety, understanding the initiating event of an accident is crucial both during its progression and in the aftermath, as it aids in consequence mitigation and post-accident management, as underscored by the Fukushima Daiichi incident. This case study explored the relationship between hydrogen production and the timeline of radioactive mass release over a 90,000-second window following two severe reactor accidents: station blackout (SBO) and SBO combined with a loss-of-coolant accident (LOCA). Four input features were used: (1) hydrogen production from zircaloy, (2) total hydrogen production, (3) radioactive mass release from fuel, and (4) radioactive mass release to the environment. The output was a categorical label indicating whether the data represented an SBO or SBO+LOCA scenario. The dataset was sourced from the study conducted by Chen et al [63].

DTIA revealed that, across all models meeting the selection criteria, the most influential feature for distinguishing between the two accident types was hydrogen production from zircaloy, followed by radioactive release from the fuel. A deeper investigation revealed that, in the SBO+LOCA scenario, most data points exceeded the 374 kg of hydrogen generated from the zircaloy cladding, as shown in Figure 10. In contrast, the majority of SBO data points fell below this threshold. To refine our understanding of the role of radioactive release, we reformulated the problem using only two input features: (1) radioactive mass release from the fuel and (2) release to the environment. DTIA then indicated that radioactive release to the environment played a more decisive role in differentiating between the two accident scenarios.

Despite using the same test size proportion and selection criteria, namely, a 20% test split, an average training–test metric difference of less than 0.01, and a minimum average test metric of 0.95, the DTC's performance declined. Analysis revealed that over half of the SBO+LOCA data points surpassed the 263 kg threshold for radioactive release to the environment. This aligns with trends reported in the source article and illustrated in Figure 11, which shows that the SBO+LOCA scenario not only results in higher overall environmental radioactive release but also initiates earlier. This observation is consistent with established literature: the presence of LOCA contributes to early radioactive buildup in the containment, which is subsequently released to the environment around the 11,000-second mark when venting occurs.

We ranked the key features identified in both problem formulations. The most representative decision tree in the first formulation had a depth of two, while the second reached a depth of three. However, our analysis of the second formulation focused only on the root and its immediate child nodes, two levels deep. The feature distributions at each node are detailed in Table 6. In formulation_1, features 0, 1, and 2 correspond to hydrogen production from zircaloy cladding, total hydrogen production, and radioactive release from the fuel, respectively. In formulation_2, features 0 and 1 represent radioactive release from the fuel to the environment. In both cases, the false branch at depth one was always a leaf node, thus containing no further features. Figure 10 illustrates that the hydrogen production threshold from zircaloy becomes meaningful only after 4000 seconds, beyond which the two accident scenarios can be easily distinguished using this threshold. This led us to formulate a key research question: what factors influence zircaloy hydrogen production in the first 4000 seconds of an accident, and how? Addressing this could improve early identification of initiating events and inform more effective accident progression control strategies.

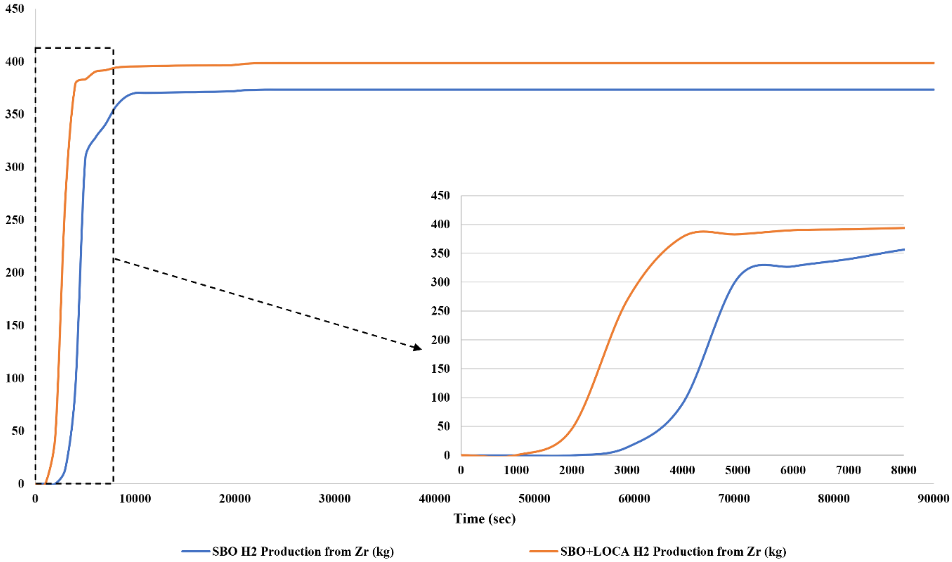

Figure 10. Hydrogen Mass Production from Zircalloy Cladding Timeline. (Taken from Paper 2 [81])

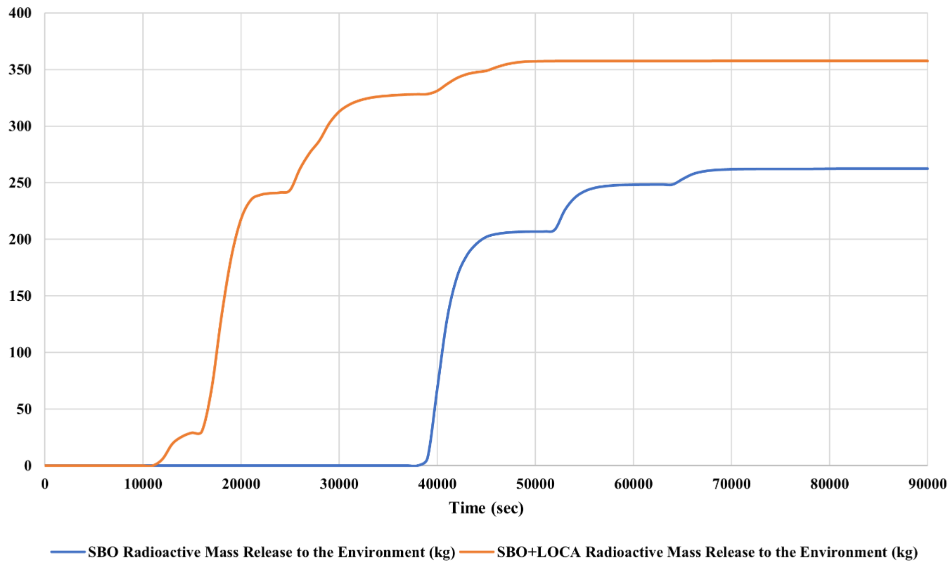

Figure 11. Radioactive Mass Release to the Environment Timeline. (Taken from Paper 2 [81])

Table 6. Significant Features and their Counts across the Developed Models. (Taken from Paper 2 [81])

	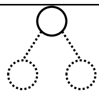		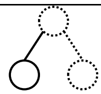		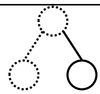	
	Depth Zero		**Depth One True**		**Depth One False**	
	Features	**Counts**	**Features**	**Counts**	**Features**	**Counts**
Formulation_1	0	1497	2	1424	NA	NA
			0	41		
			1	32		
Formulation_2	1	607	0	607	NA	NA

2.3.2 Case Study II: RNA Sequencing for Neurodegenerative Diseases in Mice

In this case study, we analysed normalised single-cell RNA sequencing data from Niemann-Pick type C1 (NPC) and healthy control mice (SRA: PRJNA606815), focusing on gene expression read counts from different cerebellar cell types [83]. Specifically, we examined astrocytes (AC) and microglia (MC). For each cell type, our method was applied twice to distinguish between healthy and diseased cells using their RNA expression profiles as input features. The dataset was divided into 80% for training and 20% for testing. Selection criteria required the average difference between training and test metrics to be under 0.1 for AC and 0.05 for MC, with minimum average test metrics of 0.9 and 0.95, respectively [81].

The average performance metrics of the evaluated models are summarised in Table 7. DTIA effectively identified key influential features from the original 27,998 input features, as shown in Table 8. Among these, feature 15075 (gene: *Lyz2*) consistently appeared at the root of all 317 models that met the selection criteria, making it the most critical gene for distinguishing between healthy and NPC-affected astrocyte (AC) cells. This gene is associated with the continuous activation of the innate immune response observed in the disease [84]. Most of the other depth-1 features had previously been linked to NPC, except for features 646 (*Itm2c*) and 14074 (*Cd81*), suggesting new potential roles in disease progression. *Itm2c* encodes Integral Membrane Protein 2C, an inhibitor of amyloid-beta production, an element known to worsen NPC when overexpressed [85]. The observed changes in *Itm2c* expression may relate to this process. *Cd81*, on the other hand, encodes a tetraspanin protein involved in halting astrocytic growth in response to neuronal signalling [86]. Increased CD81 expression in reactive astrocytes typically follows microglial (MC) activation, which is known to occur early in NPC progression, before any visible changes in astrocytes.

As expected, microglia (MC) exhibited the highest number of identified features (Table 8), reflecting the diverse physiological changes these cells undergo. Most features identified at depths 0 and 1 had been previously detected in both bulk and single-cell RNA sequencing studies from the same mouse model [87]. The low identification rate of *Lyz2* in MC (0.2%) compared to AC (100%) aligns with its biological role. Historically, *Lyz2*, also known as *LysM*, has been a key marker for distinguishing MC and other myeloid cells due to its consistently high expression in these populations [88,89]. The remaining features identified in MC align with their known transition into a disease-associated microglia phenotype, a pattern observed in several neurodegenerative disorders, including NPC1. However, the exact contribution and dynamics of this phenotype in disease progression remain unclear and may vary by stage [89]. One newly identified feature, 10130 (gene: *Shfm1*), encodes a proteasome subunit, hinting at altered protein degradation pathways in MC. While novel in this context, its appearance is consistent with the heightened phagocytic activity seen in MC from NPC mice.

Table 7. Selection and Average Metrics of the Analysed Models that Passed the Selection Criteria. (Taken from Paper 2 [81])

	Training				**Test**			
	Precision	**Accuracy**	**F1-Score**	**Recall**	**Precision**	**Accuracy**	**F1-Score**	**Recall**
AC	0.91	0.91	0.91	0.91	0.91	0.91	0.91	0.91
MC	0.97	0.97	0.97	0.97	0.96	0.95	0.95	0.95

Table 8. Significant Features in the Developed Method and Random Forest. (Taken from Paper 2 [81])

	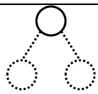		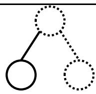		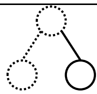			
	Depth Zero		**Depth 1 True**		**Depth 1 False**		**Random Forest**	
	Features	**Counts**	**Features**	**Counts**	**Features**	**Counts**	**Features**	**Weight**
AC	15075	317	12354	304	15148	8	15075	0.015
			20703	12	16165	26	14057	0.013
			16542	1	26599	9	11991	0.012
					11991	83	12354	0.011
					3321	1	3449	0.01
					14057	177	17343	0.009
					646	3	7893	0.009
					14074	8	20703	0.008
					3167	1	26582	0.008
					16166	1	16165	0.008
							16166	0.007
							26599	0.006
							16542	0.006
N	**317**		**317**		**317**		**0.122**	
NT	**317**		**317**		**317**		**1**	
MC	14057	427	5176	308	15075	119	17343	0.012
	5176	523	22919	49	12685	44	14057	0.011
	12354	85	14057	170	13582	39	15075	0.01
	17343	28	12354	161	1993	63	12354	0.01
	15075	5	22590	119	3167	32	12685	0.009
	12685	1	17343	13	5131	34	11991	0.009
			7838	12	6349	29	22590	0.009
			10130	28	14057	66	5176	0.009
			15210	59	9971	16	23391	0.008
			3449	22	25106	41	27346	0.008
			12685	11	18521	42	16490	0.008
			15225	13	5766	24	3167	0.007
			11313	18	14245	29	3931	0.007
					21569	75	25203	0.007
					21956	16	21834	0.007
					25348	17	15225	0.006
					11991	14	19870	0.006
					7483	13	12237	0.006
					5176	10	14894	0.006
N	**1069**		**983**		**709**		**0.149**	
NT	**1069**		**1069**		**1069**		**1**	

2.3.3 Case Study III: RNA Sequencing for Staging of Breast Cancer in Humans

The TNM system is a widely adopted framework for tumour staging, helping clinicians assess tumour status and guide treatment decisions [90]. It is a numerical system based on three components: *T* for tumour size and local tissue invasion, *N* for the number of regional lymph nodes affected, and *M* for distant metastasis (with M0 indicating no distant spread and M1 indicating the presence of metastases). While effective in many contexts, the TNM system has notable limitations. Its interpretation can be subjective and may vary due to differences in technical procedures, and its application is not consistent across all cancer types. Often, TNM classifications are grouped into simplified stages ranging from 0 to IV, where higher stages reflect more advanced and aggressive disease [91]. Importantly, the TNM system is designed specifically for solid tumours and is not suitable for certain cancers, such as leukaemia [92].

Transcriptomic data offer valuable insights into gene expression patterns in cancer, aiding our understanding of the molecular mechanisms driving tumour development and progression [93]. However, while such data can highlight tumour hallmarks and inform therapeutic strategies, it is not currently considered a reliable tool for clinical tumour staging. In this case study, we explored the relationship between RNA sequencing data and breast cancer stages in humans. Initially, we structured the problem with RNA read counts as numerical input features and cancer stages (I, II, III, or IV) as categorical outputs. The resulting models performed poorly, with accuracy metrics below 60%, failing to meet the selection criteria. To improve performance, we reformulated the problem by grouping stages I and II as stage A, and stages III and IV as stage B. This simplification led to improved model performance, exceeding 75%. Yet, analysis of the 132 models that met the criteria revealed no consistent features; each model relied on different input RNAs at different decision points. This lack of feature consistency suggests that no strong RNA markers were driving the models. We hypothesise that with a larger sample size, significant RNA features might emerge; however, we currently lack sufficient statistical evidence to support this claim.

We explored the possible reasons behind DTIA's limited performance in this case study. Breast cancer is known for its high heterogeneity, and the tumour staging labels used here, derived from histological slides, are subject to interobserver variability, as they can differ between pathologists (Histologic Grading of Breast Carcinoma: A Multi-Institution Study of Interobserver Variation Using Virtual Microscopy – PMC). Additionally, breast tumours exhibit substantial spatial variability in cellular composition, meaning the region sampled for RNA sequencing may not align with the region used for histological assessment. Moreover, each sample originates from a different patient, introducing inter-patient genetic heterogeneity, which further complicates transcriptome-wide comparisons.

2.4 Highlights on the Differences between DTIA and the Random Forest's Feature Importance Attribute

In DTIA, decision trees are trained independently from scratch using various hyperparameter settings across multiple folds. From the trees that meet predefined performance criteria, we extract key features and their corresponding threshold values. This detailed output allows researchers to gain a deeper, more interpretable understanding of the parameters that distinguish between different classes. In contrast, the random forest algorithm builds numerous decision trees using random subsets of features and samples. As a result, individual trees may perform well in some areas and poorly in others, but the ensemble generally covers the entire feature space. The algorithm then calculates feature importance based on the aggregated information gain across trees. While this metric is useful in practice, it lacks the detailed interpretability needed for physical insights, such as the specific thresholds used for splits, the feature's location within the tree, and its role in identifying a particular class. To highlight these differences, we used Case Study II to compare the interpretability and insight provided by DTIA versus the feature importance attribute from random forests.

2.4.1 AC Cell Type Classification

In Table 8, feature 16542 was identified by both DTIA and the random forest's feature importance metric. However, in DTIA, it appeared only once across the 317 models that met the selection criteria, while in the random forest, it ranked 12th overall with an importance score of 0.006. Upon examining the specific DTIA model where this feature was used, we found it had little impact on reducing the number of unhealthy samples, suggesting limited significance. This likely explains why it appeared so infrequently in DTIA results. In contrast, the random forest assigned it the same importance as feature 26599, which was detected in DTIA with a frequency of 9 out of 317 models and demonstrated greater effectiveness in distinguishing between the two classes, as shown in Table 9.

As shown in Table 9, feature 16542 helped separate healthy samples, with 98% following the true branch based on its threshold. However, it was less effective for the unhealthy group, which split nearly evenly, 41% to the true branch and

59% to the false. In contrast, feature 26599 showed stronger discriminatory power, separating healthy and unhealthy classes with average branching ratios of 80/20 and 20/80, respectively. This balanced split highlights its greater significance in distinguishing between the two classes. Feature 26599, known as *Ttr*, exhibited positive median expression in both conditions, reinforcing its relevance. Moreover, *Ttr* is also upregulated in Alzheimer's disease, further supporting its biological importance [94]. Conversely, feature 16542 (*Agt*) lacked such consistency. These findings suggest that while the random forest's feature importance metric can highlight influential features, it may fall short in capturing their deeper physical or biological significance.

Table 9. Significance of Features with Similar RF Importance Derived from the Proposed Method. (Taken from Paper 2 [81])

Number of Samples before split		Feature	RF Importance	Number of Samples After Split			
Class Healthy	Class Unhealthy			Class Healthy		Class Unhealthy	
				True	False	True	False
331	59	16542	0.006	323	8	24	35
				98%	2%	41%	59%
18	137	26599	0.006	15	3	25	112
				83%	17%	18%	82%
18	137	26599	0.006	15	3	25	112
				83%	17%	18%	82%
19	132	26599	0.006	16	3	29	103
				84%	16%	22%	78%
21	139	26599	0.006	17	4	27	112
				81%	19%	19%	81%
20	141	26599	0.006	15	5	27	114
				75%	25%	19%	81%
19	132	26599	0.006	14	5	26	106
				74%	26%	20%	80%
19	138	26599	0.006	16	3	28	110
				84%	16%	20%	80%
21	153	26599	0.006	17	4	34	119
				81%	19%	22%	78%
19	140	26599	0.006	15	4	25	115
				79%	21%	18%	82%
20	141	26599	0.006	16	4	29	112
				80%	20%	21%	79%
Average Values for Feature 26599 using the Proposed Method							
19.4	139			15.67	3.89	27.78	111.44
				80%	20%	20%	80%

2.4.2 MC Cell Type Classification

In the classification of the MC cell type, we observed more pronounced differences between the feature importance rankings derived from the random forest (RF) algorithm and those from our proposed DTIA method. These discrepancies were most evident at the root node, the point of maximum information gain, as detailed in the MC section of Table 8. Based on DTIA, the root node feature rankings were: 1) 5176, 2) 14057, 3) 12354, 4) 17343, 5) 15075, and 6) 12685. This order reflects the frequency with which each feature appeared at the root across all DT models that passed the selection criteria. In contrast, the RF feature importance produced a different ranking: 1) 17343, 2) 14057, 3) 15075, 4) 12354, 5) 12685, and 6) 5176. We presented the RF ranking until it included all the features identified by DTIA, highlighting the variation in how each method prioritises feature relevance.

We identified two additional features (1191 and 22590) with importance comparable to feature 5176. As previously noted, discrepancies existed between the feature rankings produced by our DTIA method and the random forest's feature importance. To determine which ranking was more robust, we computed the information gain for each feature using Equation 3; the higher the information gain, the greater the feature's influence at its specific threshold. These calculations are detailed in Table 10. For a more precise visualisation, Figure 12 presents scatter plots of the MC cell dataset for each feature ranked by both DTIA and the random forest, with subplot titles indicating the corresponding threshold impacts. The DTIA rankings aligned closely with the information gain results, supporting the robustness of the findings.

Table 10. Information Gain for Different MC Features at the Root Node. (Taken from Paper 2 [81])

Feature	Threshold	Below Threshold			Above Threshold			Information Gain
		N Healthy	N Unhealthy	Gini impurity	N Healthy	N Unhealthy	Gini Impurity	
5176	0.5	75	19	0.323	3	437	0.014	0.182
14057	46.5	75	19	0.323	3	437	0.014	0.182
12354	14	71	15	0.288	7	441	0.031	0.177
17343	19.5	74	20	0.335	4	436	0.018	0.176
15075	5.5	65	11	0.248	13	445	0.055	0.167
12685	31.5	62	8	0.202	16	448	0.067	0.165

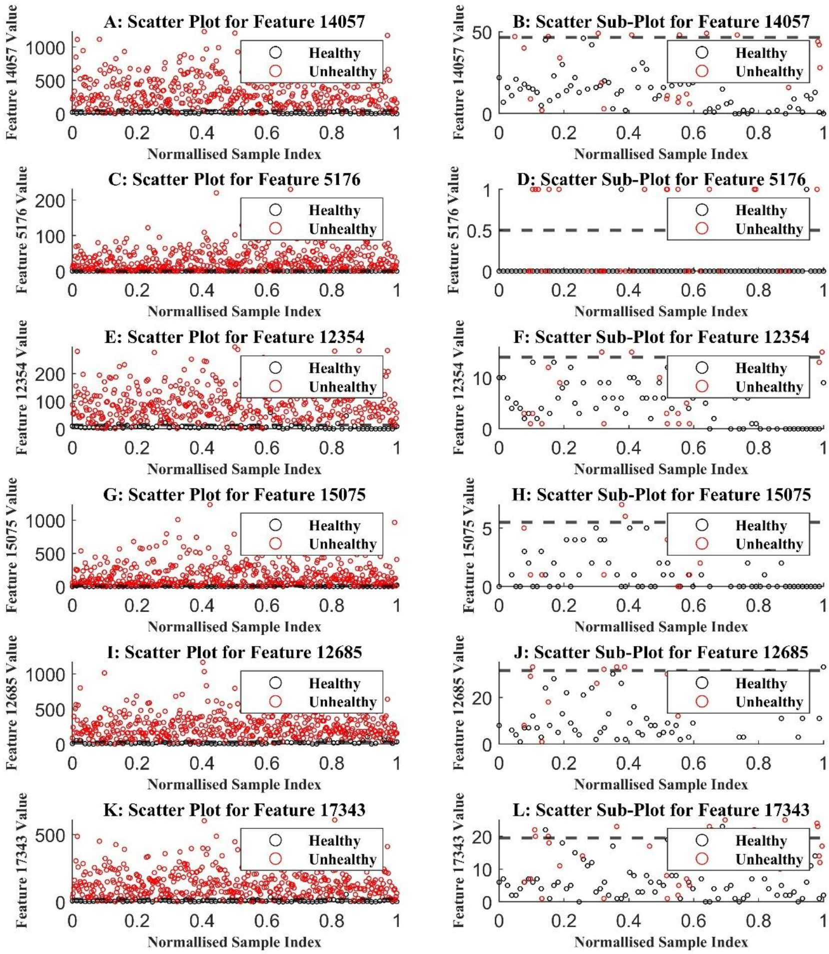

Figure 12. DTIA's Root Node Features and their Associated Thresholds for MC Cells. (Taken from Paper 2 [81])

2.5 Problem Formulations using DTIA

Previously, we discussed how DTIA can be applied to extract insights from basic classification problems in different fields of study. However, DTIA is highly dependent on the problem formulation, as seen in case study I in the previous section. Hence, in this section, we will demonstrate how DTIA can be utilised for two different types of problems: 1) time-series analysis for nuclear reactor severe accident (SA), and 2) nodal solution analysis of reactor pressure vessel (RPV) lower head at the time of failure for different SAs. In general, DTIA has eight hyperparameters that affect the insights and the computational time needed for the problem. Table 11 lists the variable names and their definitions.

Table 11. DTIA's Hyperparameters Variables Definition.

Variable	Description
test_percent	The percentage of the dataset is taken as a test dataset.
min_s_leaf_inc	Minimum number of samples per leaf increment.
min_s_leaf	Maximum number of samples per leaf.
max_depth_inc	Maximum tree depth increment.
max_depth	Maximum depth of the developed DTC.
number_of_folds	Number of folds for cross-validation.
metrics_diff	Difference between training and test precision metrics for the developed models.
avg_tst_metrics	Developed models' average performance on the test dataset.

2.5.1 Time-Series Analysis for Nuclear Reactor Severe Accident Progression

Time-series analysis using DTIA can be somewhat challenging in general due to two challenges. 1) DTIA needs labels; hence, labelling a time-series can be tricky, and 2) DTIA, being a greedy algorithm, will always report in non-consistent insights that passed the prespecified selection criteria. To resolve the first challenge, we divided the time series into four time windows based on the main events that occurred during the severe accident progression reported in the literature [63]. Reported time windows were: 1) T1: 0-6183 seconds, 2) T2: 6183-11131 seconds, 3) T3: 11131-24863 seconds, and 4) T4: 24863-90000 seconds. The 0, 6183, 11131, 24863, 90000 seconds time setpoints correspond to the onset of the accident, core support plate failure, containment venting, reactor pressure vessel's (RPV) lower head failure, and the end of the accident simulation time, respectively. We combined DTIA with the feature elimination approach to extract all possible combinations of variables associated with different time windows, while retaining the hyperparameters of DTIA listed in Table 12. In the feature elimination approach, after each run of DTIA, we remove the extracted features and rerun the DTIA over the data without the features extracted in the previous round.

To address the second challenge, we tried two different approaches when adjusting the hyperparameters of DTIA: 1) approach 1: Being graceful with the tree depth, and 2) approach 2: fixing the depth of the tree. The two approaches can be controlled by adjusting the maximum tree depth in the DTIA hyperparameters, with Approach 1 having a maximum tree depth of 15 and Approach 2 having a maximum tree depth of 2. Given that the time series is divided into four time windows (4 classes), the minimum number of rules to separate the four classes is three. Hence, the maximum tree depth of two will provide the minimum number of rules, resulting in consistent insights as shown in Figure 13. Table 13 shows the differences between the number of features extracted from each approach. It is noted that Approach 2 significantly reduced the number of extracted variables. To test the quality of the extracted insights (variables and their associated thresholds), Figure 14 illustrates the impact of the different approaches on the extracted variables. Figure 14.A shows that the threshold line, variable curve and the time setpoint do not intersect at the same point. On the other hand, Figure 14.B shows a clean intersection point between the variable, extracted threshold and the time setpoint. Hence, the insights extracted from Approach 2 reflect the high correlation between the variable and the time window.

Table 12. DTIA Hyperparameters for Approach 1 and Approach 2.

Hyperparameter	**Value**	**Hyperparameter**	**Value**
		Approach 1	
min_s_leaf_inc	10	test_percent	0.2
min_s_leaf	100	number_of_folds	10
max_depth_inc	2	metrics_diff	0
max_depth	15	avg_tst_metrics	1
		Approach 2	
min_s_leaf_inc	10	test_percent	0.2
min_s_leaf	100	number_of_folds	10
max_depth_inc	1	metrics_diff	0
max_depth	3	avg_tst_metrics	1

Table 13. Number of the Extracted Features for Each Location for Approach 1 and Approach 2.

	Number of Extracted Features			
	Root Node	**Depth 1 Nodes**	**Depth 2 Nodes**	**Total**
Approach 1	714	258	415	1387
Approach 2	33	37	63	133

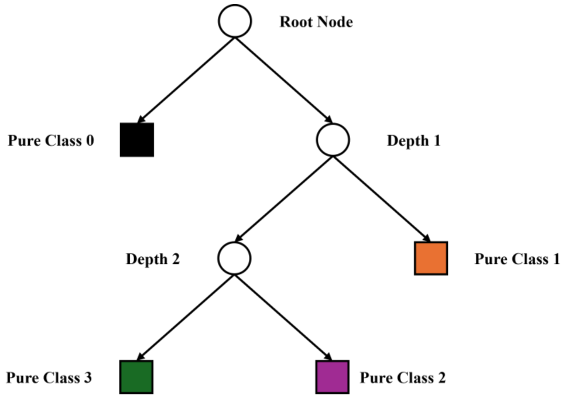

Figure 13. Three-Level Schematic of a Decision Tree for Pure Features and Thresholds Cutoff. Circles Denote Splitting Nodes and Squares Denote Pure Leaves Representing a Particular Time Window. (Taken from Paper 3)

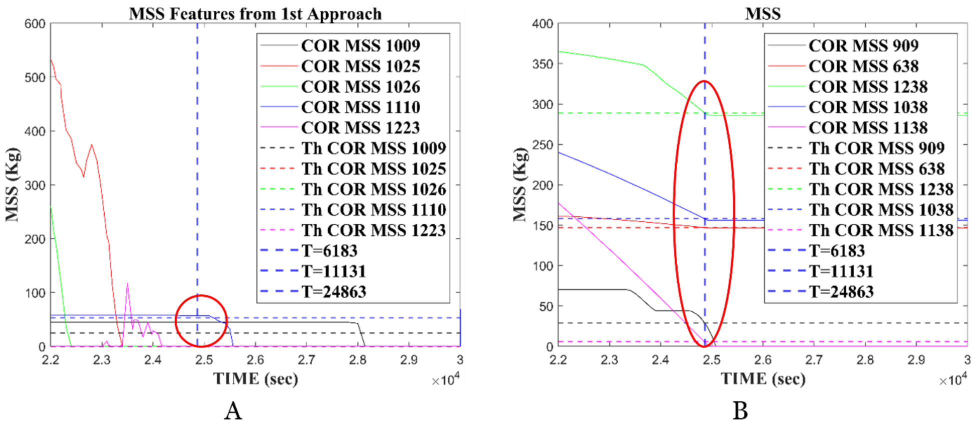

Figure 14. MSS Extracted from (A) Approach 1 and (B) Approach 2. (Taken from Paper 3)

2.5.2 Nodal Solution Analysis for Reactor Pressure Vessel's Lower Head at Time of Failure during Different SA Scenarios

We used DTIA to compare the Nodal Finite Element Analysis (FEA) solution results of the RPV's lower head for a Nordic boiling water reactor at the time of failure for two different accident scenarios. 1) Station Blackout (SBO) and 2) SBO in the presence of a loss-of-coolant accident (SBO+LOCA). The times of failure of the RPV's lower head for the SBO and SBO+LOCA accidents were previously calculated from the same ANSYS FEA model to be at 24480 and

25560 seconds, respectively [73]. The input features to DTIA were 81 nodal solution variables, and the categorical classes were SBO and SBO+LOCA accidents. In this formulation, we combined DTIA with the feature elimination approach. However, after the second round, DTIA was unable to find models that met the original selection criteria, as listed in Table 14. The nodal solution data represented 65427 and 67582 nodes for SBO and SBO+LOCA, respectively. The aforementioned nodes are the nodes that did not pass through the element-killing process because they exceeded the melting temperature of 1789 K.

Table 14. DTIA Hyperparameters Applied for Nodal Solution at RPV's Time of Failure for SBO and SBO + LOCA Accidents. (Taken from Paper 4)

Hyperparameter	**Value**	**Hyperparameter**	**Value**
	Round 1		
min_s_leaf_inc	500	test_percent	0.2
min_s_leaf	10000	number_of_folds	9
max_depth_inc	5	metrics_diff	0.05
max_depth	20	avg_tst_metrics	0.95

2.6 K-Means Clustering Guided Decision Tree Insights Analytics (DTIA) Framework

Despite the extensive information provided by DTIA, it has two main limitations: 1) the pattern between inputs and categorical outputs must be modelable using DTCs, as DTCs form the backbone of DTIA. 2) Data must be categorised (labelled) before being fed into DTIA. In this section, we tackled the second limitation. We added a clustering step before feeding the complete dataset to DTIA. In other words, input features are fed to a clustering algorithm, which labels the samples according to the similarities found. Then, both the input features and the assigned labels are fed to DTIA for information extraction. We chose K-Means as the clustering algorithm, as it can be explained.

2.6.1 Overview of K-Means Clustering

K-means clustering is a type of unsupervised learning in the field of machine learning. Unsupervised learning aims to cluster the samples in a given dataset into groups with common characteristics (features) [79]. The main difference between unsupervised learning and supervised learning is that unsupervised learning does not have targets for the input features. Hence, clustering aims to assign arbitrary labels to the samples with similar characteristics. However, knowing the number of labels that a dataset can be divided into can be challenging. Nevertheless, clustering serves a crucial role in exploratory analysis. Exploratory data analysis aims to identify patterns in different categories, revealing commonalities. Identified patterns are then projected onto the domain of knowledge to extract insights.

K-Means clustering is a distance-based clustering algorithm that is randomly initiated. Assuming there is a dataset consisting of n samples, where each sample consists of m dimensions. Depending on the required number of clusters, the K-means algorithm initiates random centroid positions in the feature space. Hence, each centroid will be of m dimensions. That said, the algorithm then starts assigning each of the n samples to one of the centroids. Each of the centroids' positions is then updated based on the samples belonging to that particular cluster. The updated centroid position is the average value of the samples belonging to the cluster over each dimension. The objective is to minimise the distances between the samples and their cluster centroid position in Euclidean space by minimising the Euclidean distance calculated using Equation 11, where $d(p, q)$ is the Euclidean distance between points p and q, while q_i and p_i are the Euclidean vectors for the i dimension ranging from one to m dimensions (features). Given that the centroid position is the average of all of its data points, the general cost function to be minimised can be written as in Equation 12, where, J is the cost function, k is the number of clusters, C_i is the set of data points assigned to a cluster i, x is a data point belonging to a cluster C_i and μ_i is the mean vector of all data points belonging to the cluster C_i (centroid position vector). Hence, $||x - \mu_i||^2$ is the squared Euclidean distance between the point x and the centroid position μ_i. K-means algorithm stops in one of three cases: 1) the data points assigned to each cluster do not change, 2) the change in the values of the position vector is below a certain threshold, and 3) a maximum number of iterations is reached. A summary of the K-Means clustering algorithm is demonstrated in Figure 15. Due to the random initiation of the centroids position, there is no guarantee of convergence. Hence, it is a common practice to run the K-Means algorithm over a high number of trials (the range of trials is problem- and data-dependent) and assign the data points to different clusters based on their majority vote [95–97].

$$d(p, q) = \sqrt{\sum_{i=1}^{m} (q_i - p_i)^2}, \qquad (11)$$

$$J = \sum_{i=1}^{k} \sum_{x \in C_i} \|x - \mu_i\|^2 , \qquad (12)$$

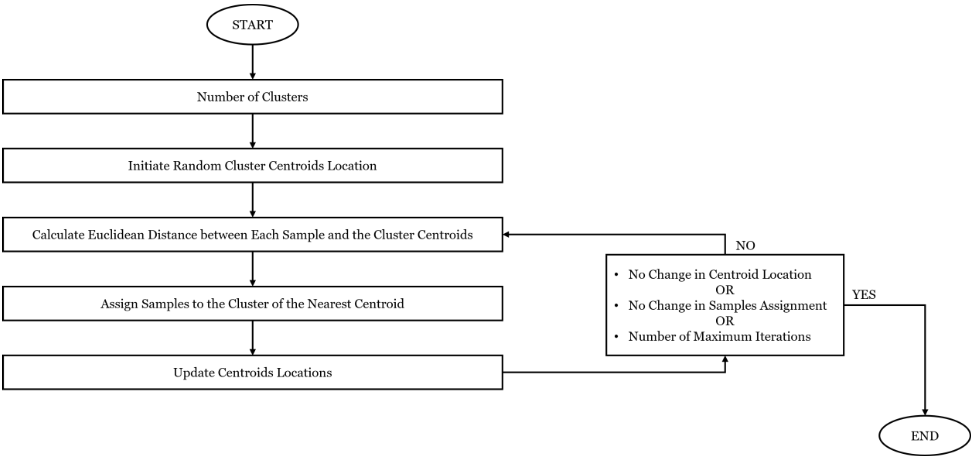

Figure 15. K-Means Clustering Implementation Flow Chart.

Building on this framework, we calculated the Euclidean distances between each feature in one centroid and its counterpart in other centroids to assess the significance of each feature (dimension) in the clustering process. By ranking these distances in descending order, we identified features with greater separation between centroids as more distinctive for specific clusters. To validate this approach, we applied K-means clustering to the biological samples, specifically MC cells, as summarised in Table 15. Here, ranks R01 to R10 indicate the order of Euclidean distances between centroids of the two classes (presumed healthy and unhealthy clusters). The numbers beside each feature denote the frequency with which that feature occupied a given rank across all trials. Each column sums to 100, reflecting the total number of K-means runs conducted, as described previously [81].

We compared the Euclidean distance-based feature ranking from K-means clustering with the feature importance from the random forest algorithm and insights from DTIA. As shown in Table 16, there are clear discrepancies between the root node features identified by DTIA and the top-ranked features from the random forest. These differences were previously explained in terms of information gain. While both DTIA and RF's feature importance include most features appearing in the K-means ranking, their order differs. Notably, K-means ranks features 11991 and 26599 as most important, yet these features are not highly ranked in DTIA or random forest results. This is likely because K-means is an unsupervised method that does not use labeled data, which can lead to less accurate feature importance. Therefore, although K-means feature ranking can offer useful insights for unlabeled data, it does not outperform DTIA or random forest feature importance when labels are available.

Table 15. Features (Dimensions) with maximum Euclidean Distance between Centroids. (Taken from Paper 2 [81])

Feature	R01	R02	R03	R04	R05	R06	R07	R08	R09	R10
11991	61				37	2				
26599	39									
14057		61								37
27913		39								
27346			61							
27914			39							
15075				61						
23119				37	2					
27910				2		37				
12685					61					
17343						61				
5131							61			
27908							37		2	
27920							2	37		
12354								61		
27911								2	37	
7893									61	
9204										61
27917										2

Table 16. Feature Ranking for the MC Cells in Case Study II according to DTIA, Random Forest, and K-Means. (Taken from Paper 2 [81])

DTIA		Random Forest		K-Means	
Feature	**Counts**	**Feature**	**Rank**	**Feature**	**Rank**
5176	523	17343	1	11991	1
14057	427	14057	2	26599	1
12354	85	15075	3	14057	2
17343	28	12354	4	27913	2
15075	5	12685	5	27346	3
12685	1	11991	6	27914	3
				15075	4
				23119	4
				12685	5
				17343	6
				27910	6

2.6.2 K-Means + DTIA Framework

As previously noted, DTIA requires pre-labelled time windows for time-series analysis. To overcome this limitation, we propose an unsupervised learning approach that labels time windows based on similarities within a high-dimensional feature space using K-Means clustering. This technique groups time points with comparable multi-dimensional patterns into distinct windows, effectively identifying unique events. K-Means assigns arbitrary labels (e.g., 0, 1, 2, etc.) to these clusters, which, along with their associated data, serve as input to DTIA with a fixed maximum tree depth. This approach ensures that the insights generated correspond directly to the clustered time windows, as illustrated in Figure 16.

To validate this framework, we initially chose four clusters to replicate the time windows identified by Chen et al [63]. However, the clustering results differed, with one cluster containing only a single time point. As a result, we reduced the number of clusters to three. In these experiments, K-Means was run 1,000 times, with each run allowing up to 1,000 iterations for centroid convergence. The final label for each time point was assigned based on the mode of labels across all runs. While machine learning pipelines can suffer from error propagation, we minimised this risk between K-Means and DTIA by carefully tuning DTIA's hyperparameters to reduce errors. With three identified time windows, DTIA was limited to a tree depth of one, as depicted in Figure 17.

To ensure robustness, we enforced strict model selection criteria demanding 100% accuracy on both training and test sets, with no difference in precision between them. Limiting tree growth under these rigorous conditions guarantees that each extracted feature and its threshold uniquely corresponds to one of the three identified time windows. While clustering methods like K-Means can introduce bias if not empirically validated, our goal was to evaluate whether this approach could reveal patterns consistent with those found in the traditional analysis by Chen et al [63]. A summary of the hyperparameters used for both K-Means and DTIA is provided in Table 17.

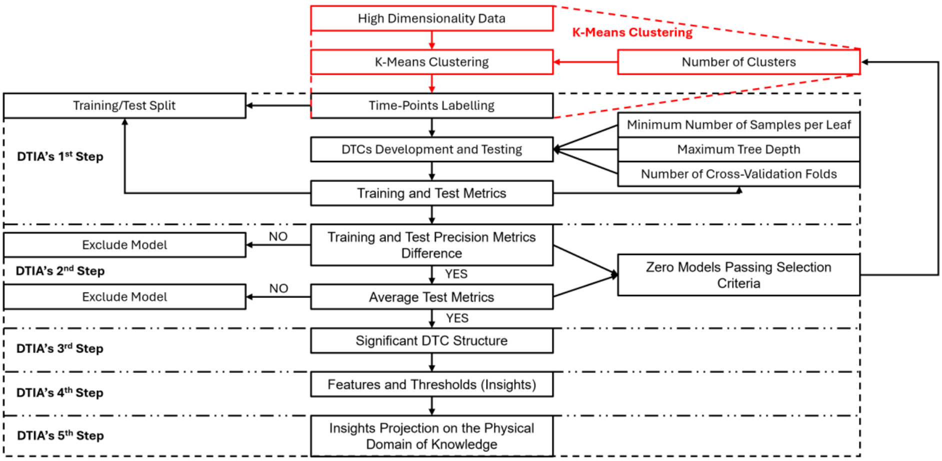

Figure 16. Summary of the Proposed Framework that Combines K-Means Clustering with DTIA. (Taken from Paper 5)

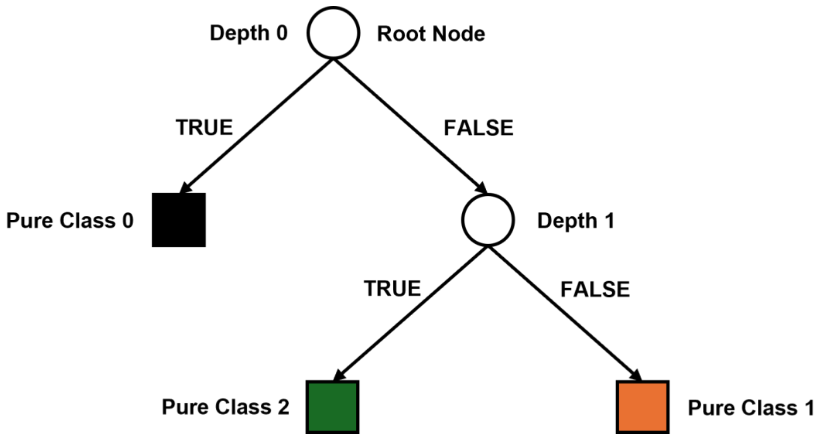

Figure 17. Minimum Tree Structure for Three-Time Windows Classification. (Taken from Paper 5)

Table 17. K-Means and DTIA Hyperparameters. (Taken from Paper 5)

Hyperparameter	Value	Hyperparameter	Value
K-Means Max Iterations	1000	Number of K-Means Runs	1000
Test (%)	20	Number of Samples per Leaf	20
Metrics Difference (%)	0	Number of Samples per Leaf Increment	1
Average Test Metrics (%)	100	Maximum Depth	2
Number of Folds	11	Maximum Depth Increment	1

3 Results and Discussion

This chapter covers the insights extracted from the application of DTIA and the K-means + DTIA framework to three different nuclear reactor safety problems. First, we applied DTIA to MELCOR's COR package time-wise results of station blackout in the presence of a loss-of-coolant accident (SBO + LOCA) in the Nordic boiling water reactor. Second, we applied DTIA to ANSYS structural variable results to extract the differences between the failure of the pressure vessel lower head at the time of failure due to an SBO and SBO + LOCA accidents. Finally, we applied the K-Means + DTIA framework to MELCOR's COR package time-wise results, where the significant time stamps were decided by the K-Means instead of being pre-defined from literature, as in the first application.

3.1 DTIA Applied to Severe Accident Time-Wise Propagation

Using Approach 2 within the DTIA framework for the time-wise propagation of SA yielded 133 dimensions strongly linked to the proposed time windows described in the previous chapter. Due to the inherent greediness of the DTC algorithm underlying DTIA, the root node dimensions were associated with the T4 window, depth one with T3, and depth two with both T1 and T2. The following section presents an interpretation of these extracted insights and their relevance to the respective time windows.

3.1.1 Root Node: Associations with T4

DTIA identified seven unique root-node dimensions strongly associated with T4, divided into two categories: (1) total and rate of decay heat generation (two dimensions) and (2) mass of the support structure (MSS, five dimensions). As shown in Figure 18, the monotonic behaviour of decay heat, total increasing and rate decreasing, naturally produced thresholds that consistently separated the time windows. Four of the five MSS dimensions corresponded to axial level 38 (the core support plate, rings 1–17), while one was linked to axial level 9. In MELCOR, the plate was modelled as a "PLATEB" support, meaning its debris-retaining function fails before it melts [63]. Figure 19 shows that MSS in rings 11 and 9 (axial levels 38 and 9) dropped sharply after T4 began, while other rings remained stable. This was further examined in Figure 20 and Figure 21, where mass and temperature profiles confirmed partial melting of the core support plate in specific rings, though not all sections failed within the 90,000-second simulation period.

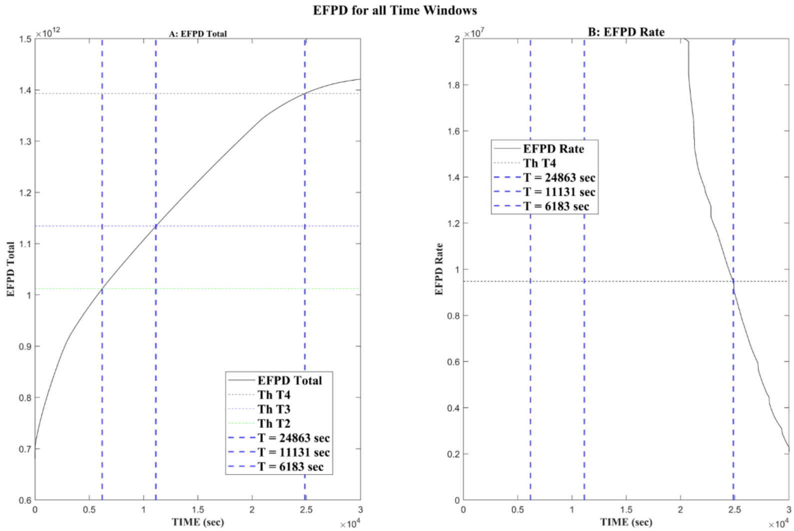

Figure 18. Decay Heat Generation, (A) Total and (B) Rate. (Taken from Paper 3)

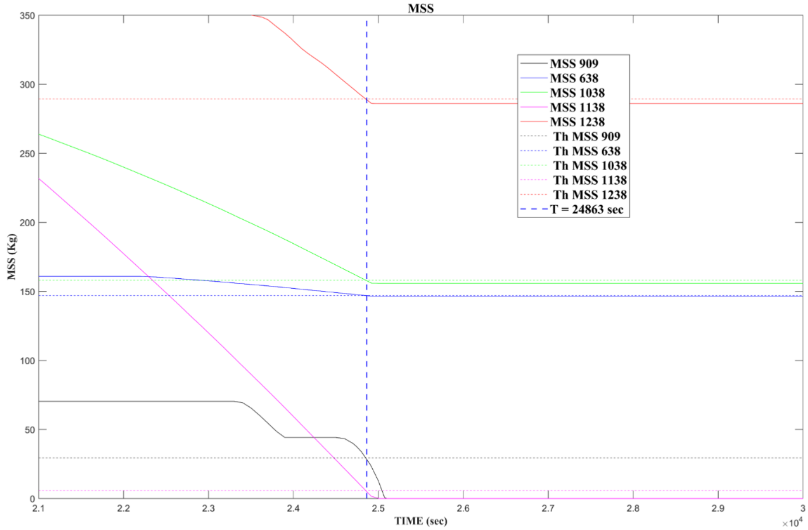

Figure 19. Mass of Stainless Steel in different cells Highlighted by DTIA in the Root Node associated with T4. (Taken from Paper 3)

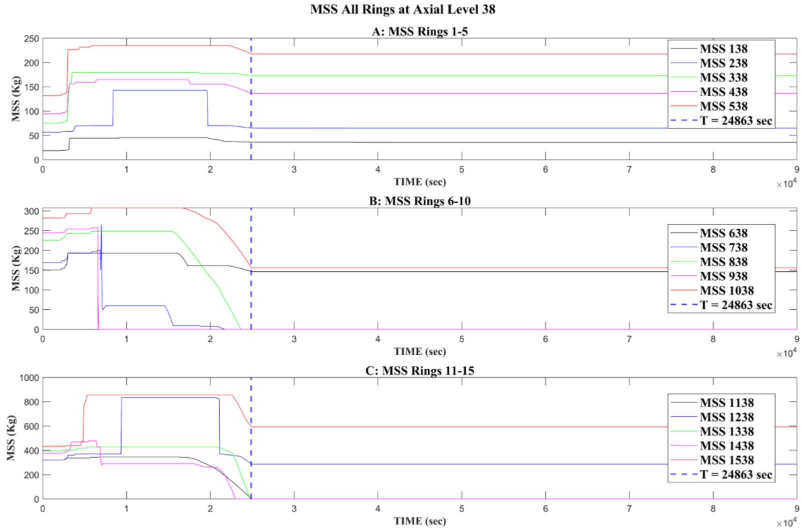

Figure 20. Mass of Stainless steel over all rings in the active core region at the core support plate axial level. (Taken from Paper 3)

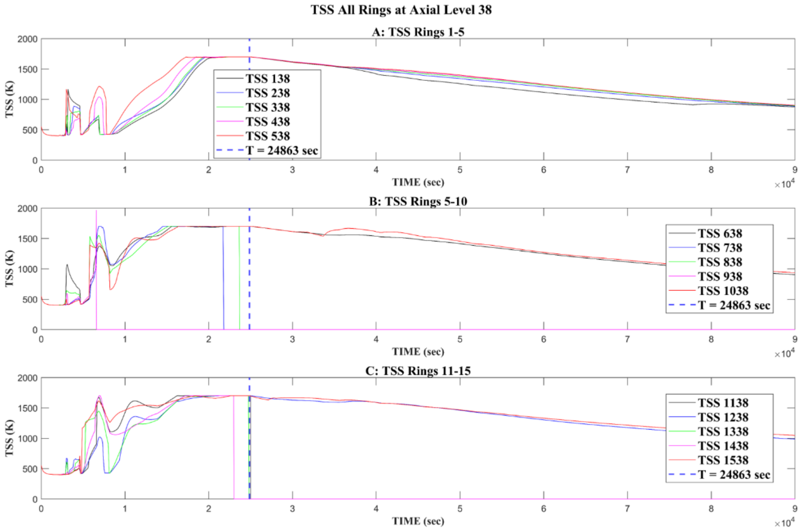

Figure 21. Temperature of Stainless Steel for all Rings in the Active Core region (Rings 1-15) at axial level 38. (Taken from Paper 3)

3.1.2 Depth 1: Associations with T3

Depth 1, derived from applying the variable rules at the root node, was strongly associated with the T3 time window and involved 30 distinct variables grouped into six categories: MSS, MUO2, MZR, TSVC, particulate debris masses (PB and PD MUO2), and global totals (decay heat, energy, and hydrogen). Among these, MSS, MUO2, MZR, and particulate debris masses provided the most informative insights, collectively pointing to significant core relocation below the core support plate (axial level 39). As shown in Figure 22.A, MSS in axial levels 41–35 nearly vanished by ~18,000 seconds, while Figure 22.B highlights the rapid depletion of MSS from axial level 39 down to 13, indicating melting or relocation into lower regions. A similar trend is observed in MUO2: Figure 23 shows mass depletion at axial level 43 in the active core, contrasted by increases at lower head levels 14, 16, and 18, consistent with fuel relocation. MZR behaviour in Figure 24 supports this hypothesis, with general decreases except for axial level 25 in the lower head. Finally, Figure 25 shows increasing particulate debris mass in lower head cells and bypass regions, particularly levels 14 and 17, confirming continued downward relocation of core materials, with uranium dioxide debris steadily accumulating as the process progressed.

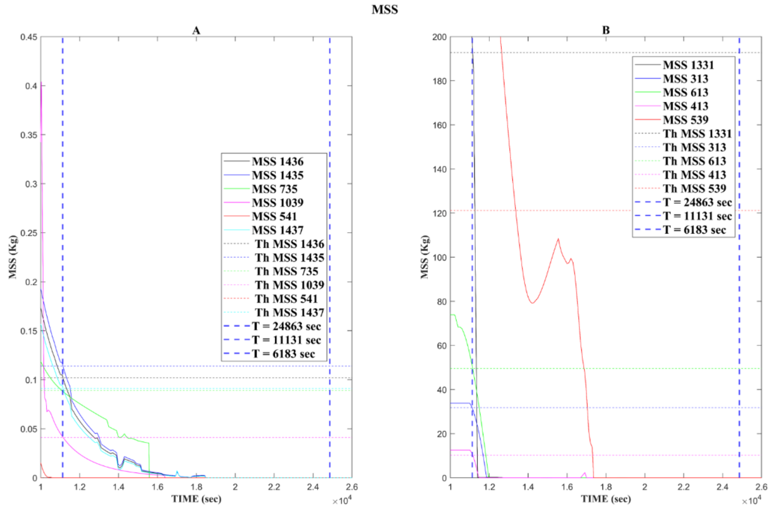

Figure 22. Mass of Stainless Steel for variables extracted by DTIA that are associated with T3. (Taken from Paper 3)

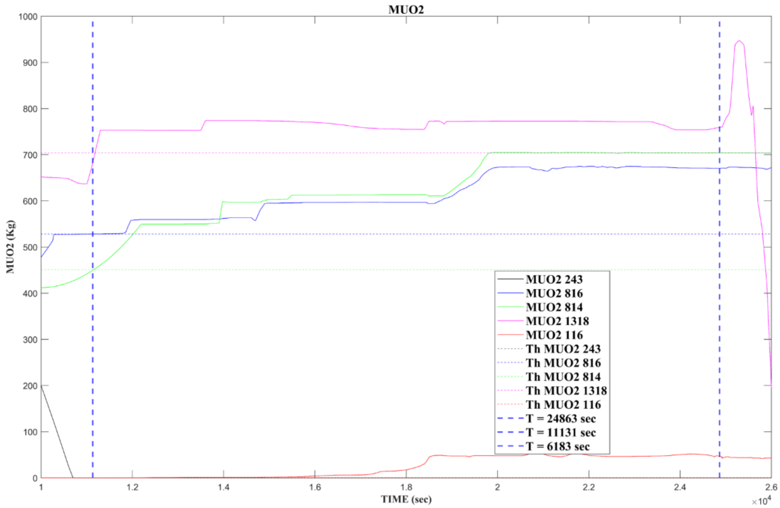

Figure 23. Mass of Uranium Dioxide for variables extracted by DTIA that are associated with T3. (Taken from Paper 3)

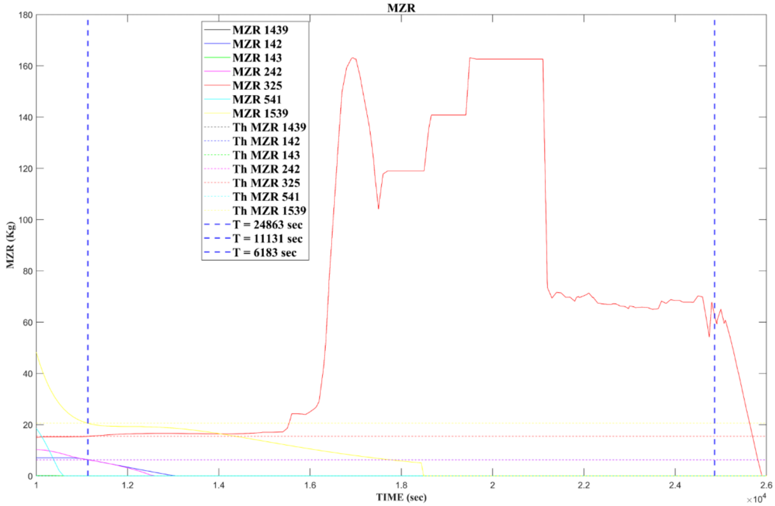

Figure 24. Mass of Zircalloy for variables extracted by DTIA that are associated with T3. (Taken from Paper 3)

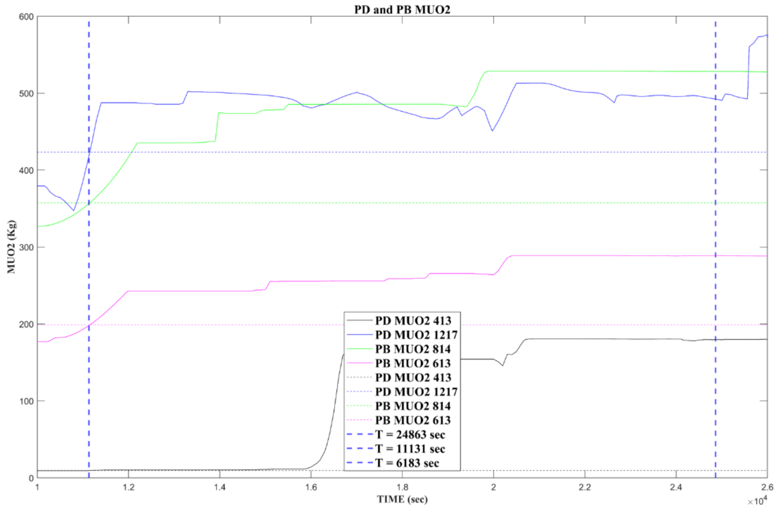

Figure 25. Mass of Particulate debris in COR cells and the bypass for variables extracted by DTIA that are associated with T3. (Taken from Paper 3)

3.1.3 Depth Two: Separating T1 from T2

Depth 2 was responsible for separating T1 from T2, with MSS, MZR, MUO2, and particulate debris variables (PD and PB MUO2) selected from DTIA for further analysis. As shown in Figure 26, the MSS variables identified by DTIA closely matched T1 behaviour, with a clear drop at axial level 40 (the lowest active core level) and a spike at axial level 12 following the core support plate failure, after which values remained stable throughout T2. However, MSS203 began increasing before the failure timestamp, suggesting an early rise in lower head mass; this was also observed in MSS204 and MSS205, though not in higher levels, challenging the assumption of relocation and warranting further investigation. Figure 27 shows a similar anomaly in MZR, where MZR1313 and MZR204 exhibited unexpected mass increases prior to plate failure, while the remaining MZR variables decreased as expected at the onset of failure. MUO2 and its particulate debris behaved consistently with expectations, as illustrated in Figure 28 and Figure 29, with active core levels showing significant mass loss at the time of support plate failure and lower levels gradually gaining mass.

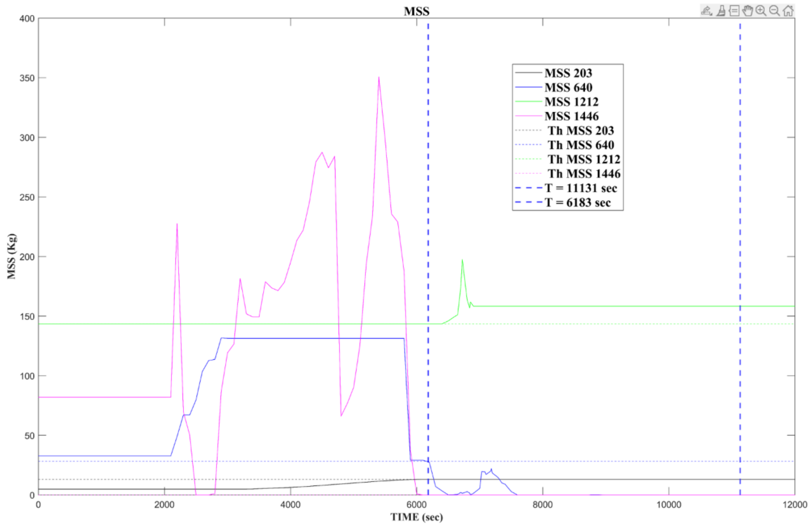

Figure 26. Mass of Stainless Steel for variables extracted by DTIA that are associated with the separation of T1 and T2. (Taken from Paper 3)

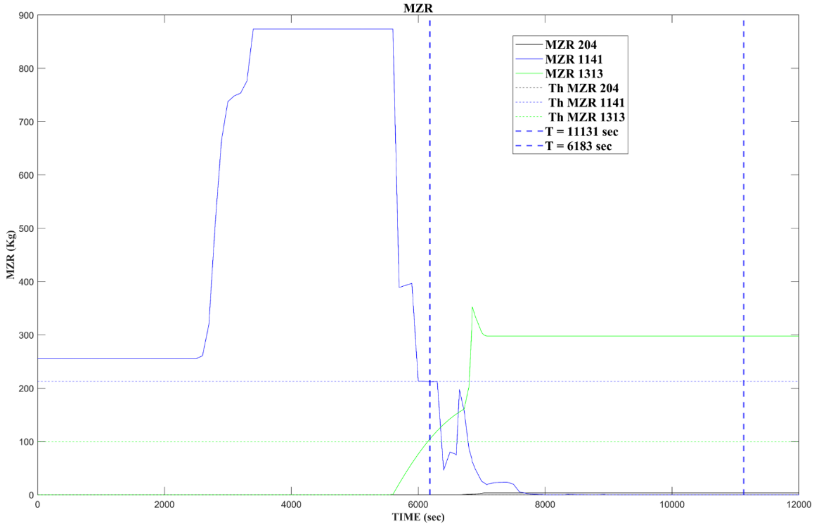

Figure 27. Mass of Zircalloy for variables extracted by DTIA that are associated with the separation of T1 and T2. (Taken from Paper 3)

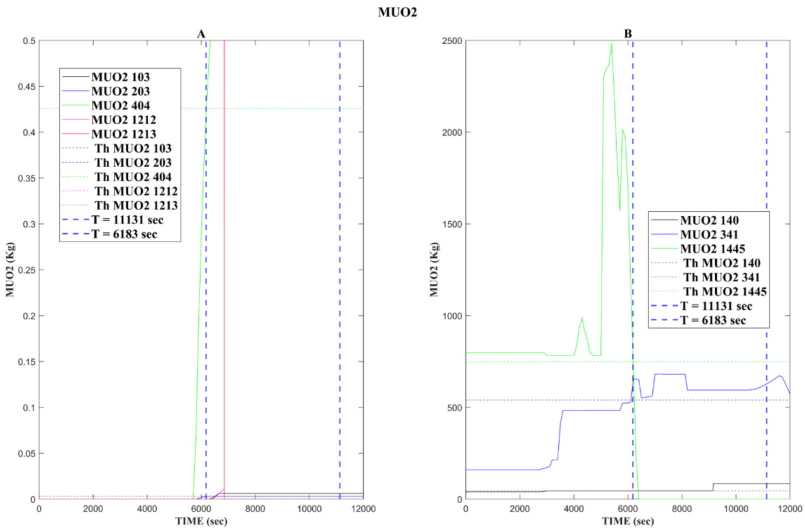

Figure 28. Mass of Uranium Dioxide for variables extracted by DTIA that are associated with the separation of T1 and T2. (Taken from Paper 3)

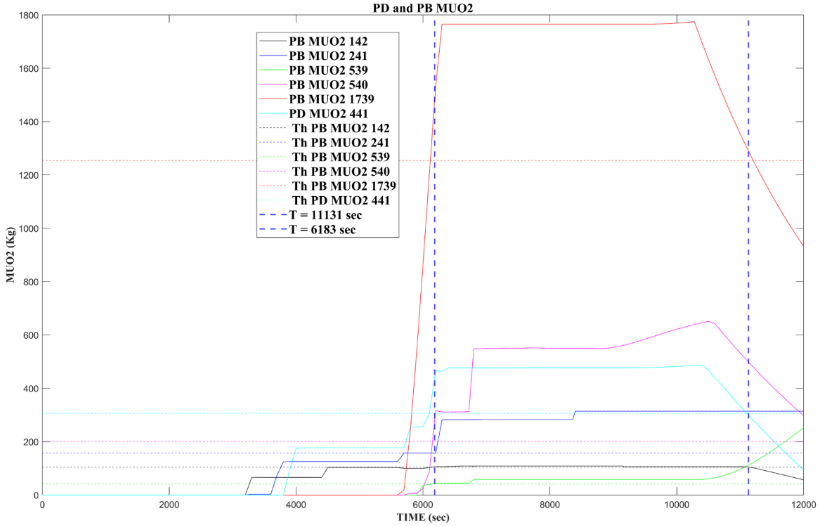

Figure 29. Mass of Particulate Debris in the Cor Cells and the Bypass for variables extracted by DTIA that are associated with the separation of T1 and T2. (Taken from Paper 3)

3.2 DTIA Applied to RPV's Lower Head Failure due to Different Severe Accidents

Applying DTIA to the RPV's lower head structural variables at the time of failure due to SBO and SBO + LOCA accidents revealed some of the similarities and differences in the two cases. Figure 30 shows the typical DTIA tree that used nine structural parameters to differentiate between the state of the RPV lower head at the time of failure for the two accidents. Each colour in the demonstrated RPV lower head sections represents a series of rules following the tree below. The combination of rules and their associated thresholds is summarised in Table 18. This particular model has been previously analysed by Wang et al [73]. Since it has been previously analysed, we have some preliminary information about the location of the failure. According to Wang et al.'s work [73], the failure region was around the same location covered by C10 and C11 [73]. The C11 final rule depended on Von-Mises stress, which is the main driver in the traditional analysis that exceeded the ultimate stress and was labelled as the main reason for failure. On the other hand, the C10 final rule relied on the hydrostatic pressure, which had never been mentioned in traditional analysis and was often overlooked, as it represents the average stress in the three directions (x, y, and z) and is calculated using equation 13. The threshold associated with hydrostatic pressure was -0.3 MPa. That said, we plotted the regions where DTIA used hydrostatic pressure and von Mises stress to differentiate between the state of the RPV lower head, as shown in Figure 31. In Figure 32, we focused on the region of failure identified earlier in Wang et al.'s work [73]. According to DTIA, the SBO case is unique in the Von-Mises stress with an inner edge of hydrostatic pressure, while the SBO + LOCA case is dominated by the hydrostatic pressure. Hence, we studied both variables for the whole region of failure as shown in Figure 33.A and Figure 33.B for Von-Mises stress and hydrostatic pressure, respectively.

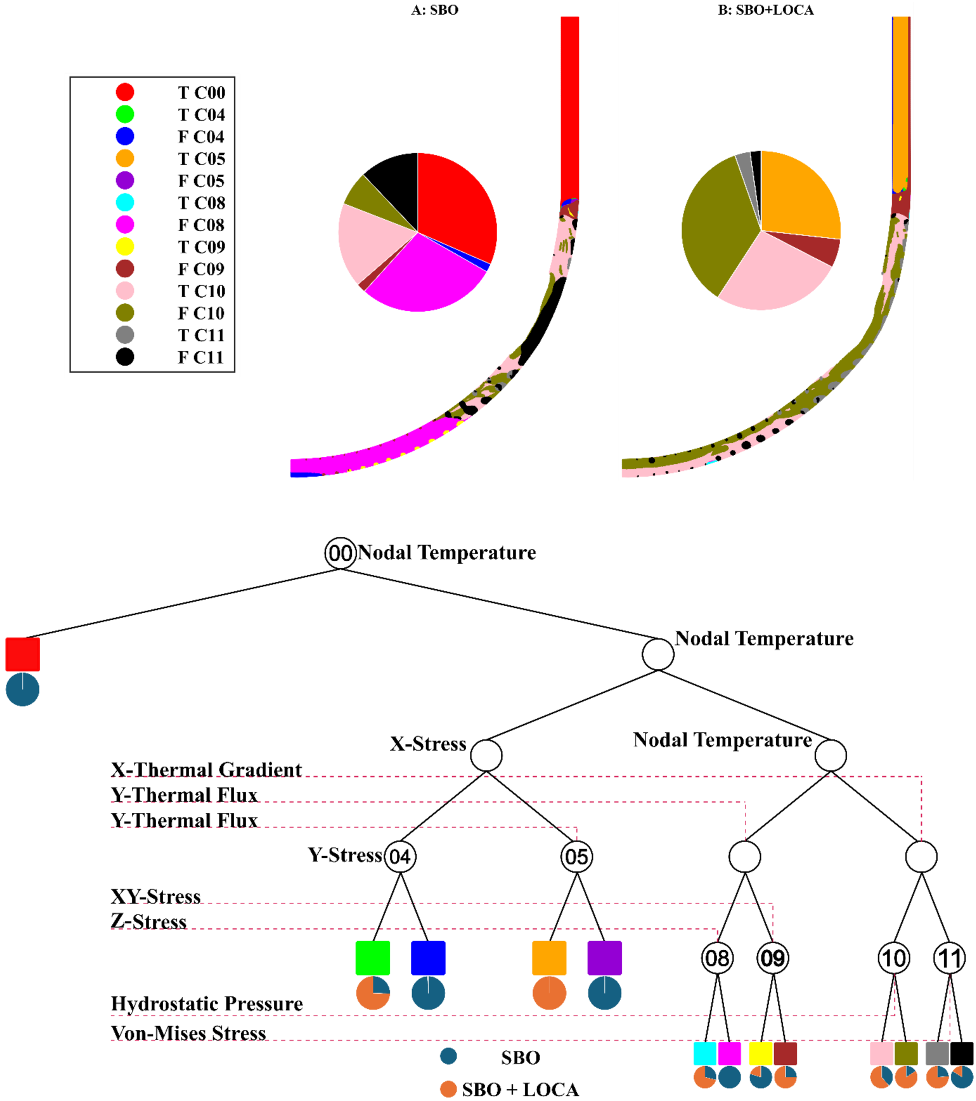

Figure 30. Top: Results of DTIA Segmentation of the Reactor Pressure Vessel. Bottom: Typical Decision Tree Extracted from DTIA. Colour Code in the Tree is the same as the Segmentation Colours. (Taken from Paper 4)

$$Hydrostatic\ Pressure = \frac{(\sigma_x + \sigma_y + \sigma_z)}{3}, \qquad (13)$$

Table 18. Combination of Rules Breakdown, where Pressure and stress in MPa, Thermal flux (W/m2), Thermal Gradient (K/m). (Taken from Paper 4)

Path	Rules
T C00	$Nodal\ Temperature \leq 488$
T C04	$488 < Nodal\ Temperature \leq 520$ $X - Stress \leq -1.13$ $Y - Stress \leq -9.21$
F C04	$488 < Nodal\ Temperature \leq 520$ $X - Stress \leq -1.13$ $Y - Stress > -9.21$
T C05	$488 < Nodal\ Temperature \leq 520$ $X - Stress > -1.13$ $Y - Thermal\ Flux \leq 18672$
F C05	$488 < Nodal\ Temperature \leq 520$ $X - Stress > -1.13$ $Y - Thermal\ Flux > 18672$
T C08	$520 < Nodal\ Temperature \leq 744$ $Y - Thermal\ Flux \leq -104$ $Z - Stress \leq 84.19$
F C08	$520 < Nodal\ Temperature \leq 744$ $Y - Thermal\ Flux \leq -104$ $Z - Stress > 84.19$
T C09	$520 < Nodal\ Temperature \leq 744$ $Y - Thermal\ Flux > -104$ $XY - Stress \leq -19.78$
F C09	$520 < Nodal\ Temperature \leq 744$ $Y - Thermal\ Flux > -104$ $XY - Stress > -19.78$
T C10	$Nodal\ Temperature > 744$ $X - Thermal\ Gradient \leq 56$ $Hydrostatic\ Pressure \leq -0.3$
F C10	$Nodal\ Temperature > 744$ $X - Thermal\ Gradient \leq 56$ $Hydrostatic\ Pressure > -0.3$
T C11	$Nodal\ Temperature > 744$ $X - Thermal\ Gradient \leq 56$ $Von - Mises\ Stress \leq 2.07$
F C11	$Nodal\ Temperature > 744$ $X - Thermal\ Gradient \leq 56$ $Von - Mises\ Stress > 2.07$

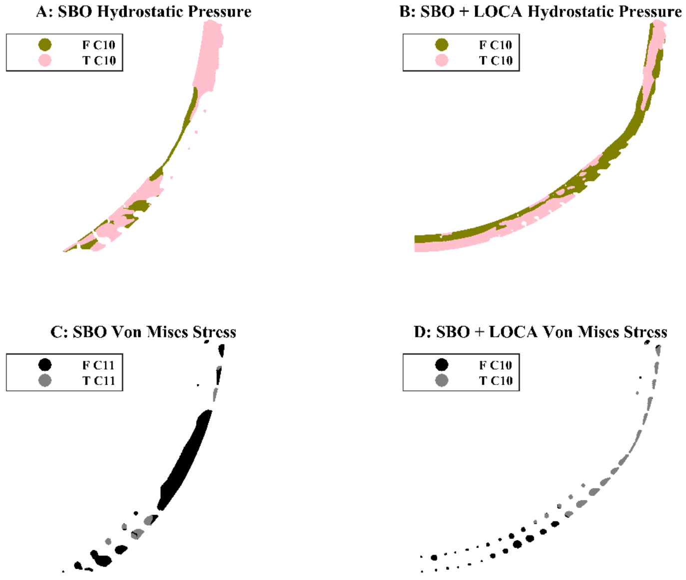

Figure 31. Hydrostatic Pressure and Von Mises Stress (Spatial Plot, not the Actual Values) based on their Contribution Governing all Nodes Following the Rules from Figure 30 and Table 18. (Taken from Paper 4)

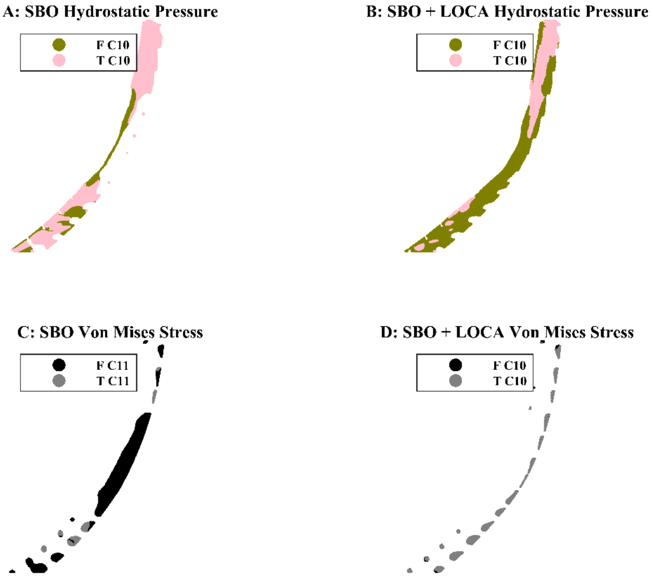

Figure 32. Hydrostatic Pressure and Von Mises Stress (Spatial Plot, not the Actual Value) Focused on the Region of Failure with Equal Dimensions. (Taken from Paper 4)

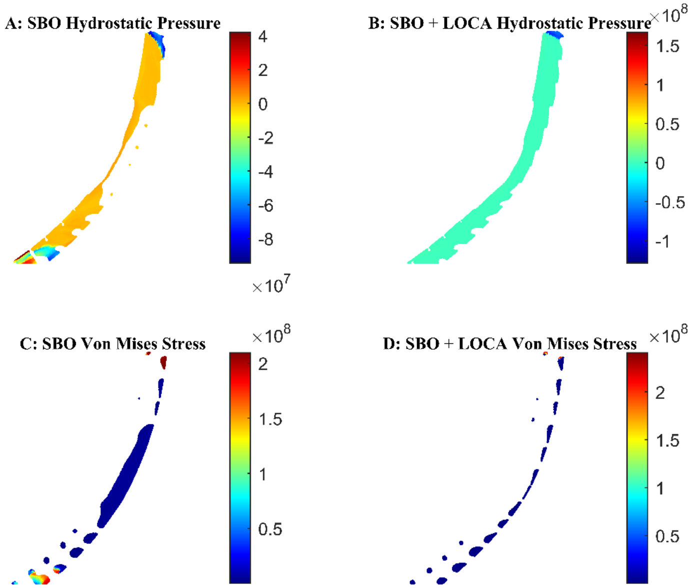

Figure 33. Hydrostatic Pressure and Von Mises Stress Values in the Failure Region According to the DTIA Segmentation. (Taken from Paper 4)

Although the threshold for the hydrostatic pressure was -0.3 MPa, we chose to study the plots from the direction point of view (positive and negative hydrostatic pressure) as shown in Figure 34. Conventionally, positive and negative hydrostatic pressure mean compressive and tensile pressure, respectively. From Figure 34, we can see that the SBO case is more dominated by tension stress, while the SBO + LOCA case is more dominated by compression stress. In general, a tension-dominated structure is more prone to cavity formation, leading to earlier failure due to crack propagation. On the other hand, compression-dominated structures lead to more buckling and deformation before going through a ductile fracture. This interpretation aligns with previously published observations about the buckling of the SBO + LOCA case being more than that of the SBO case [73]. This also aligns with the time of failure due to stress that SBO + LOCA fails at around 25560 seconds (7.1 hr), while the SBO case fails at 24480 seconds (6.8 hr), 0.3 hr earlier than the SBO + LOCA case. Given that the temperature at the SBO + LOCA case was higher than the SBO case, as shown in Figure 35, this supports the later failure time. However, to study this from another dimension, we plotted the thermal gradient of the region of interest as shown in Figure 36. X-thermal gradient shows a much higher positive gradient in the SBO case compared to the uniform negative gradient in the SBO + LOCA case. In addition, the Y-thermal gradient shows a kind of uniform high-to-low gradient in the SBO + LOCA case compared to the discontinued patches in the SBO case. The high X-thermal gradient and the discontinuous patches of high Y-thermal gradient enhance the tension-dominated hydrostatic pressure behaviour in the SBO case, supporting the interpretation of the earlier failure of the SBO case compared to the SBO+ LOCA case.

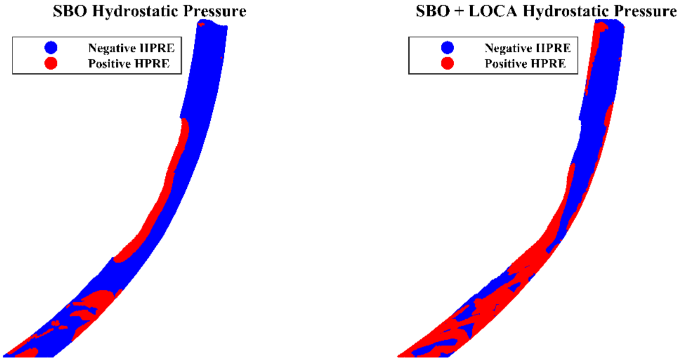

Figure 34. Positive and Negative Hydrostatic Pressure in the Region of Failure. (Taken from Paper 4)

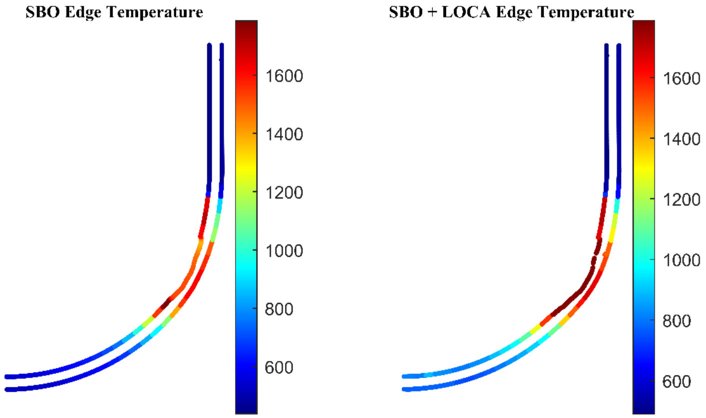

Figure 35. Edge Temperature Plot at the Time of Failure after Applying the Element-Killing Treatment due to Exceeding the Melting Temperature. (Taken from Paper 4)

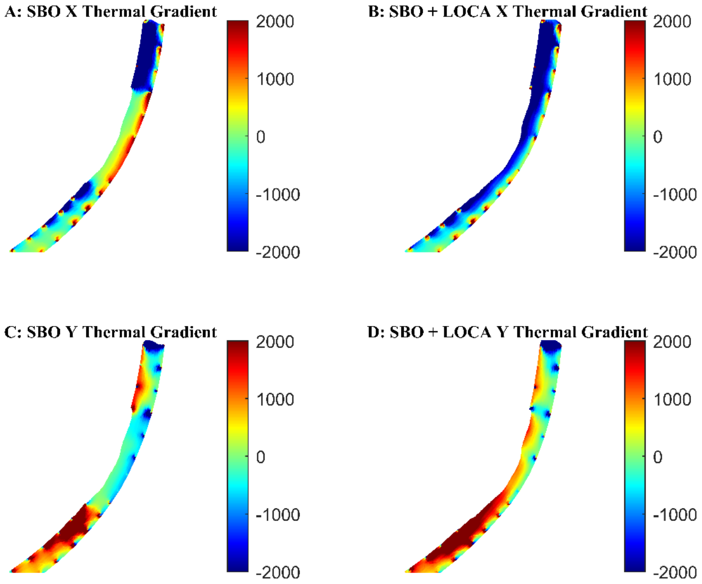

Figure 36. Thermal Gradient in the Region of Failure. (Taken from Paper 4)

3.3 DTIA + K-Means Applied to Severe Accident Time-Wise Propagation Staging

K-means clustering identified two separation points at 5900 and 17,511 seconds, dividing the 90,000-second timeline into three intervals: 0–5900 seconds (62 time points), 5900–17,511 seconds (208 time points), and 17,511–90,000 seconds (503 time points). For clarity, these intervals are hereafter referred to as T1 (majority in 338/1000 iterations), T2 (355/1000 iterations), and T3 (356/1000 iterations). DTIA analysis showed that 154 of the 220 developed models achieved perfect training and testing performance, relying on 118 of the original 23,950 COR package dimensions. Among these, T3 was consistently separated at the root node, with 29 parameters strongly associated with it—an expected outcome given its larger number of points and resulting higher information gain. T1 and T2 were then separated at the next depth, revealing 94 distinguishing parameters. Notably, the time windows suggested by K-means differ from those reported in Chen et al. [63], which we attribute to two factors: (1) containment venting, emphasised in the earlier analysis, is weakly correlated with the COR package results, and (2) the K-means-derived timestamps highlight the strongest statistical associations. We anticipate that integrating a feature elimination strategy into the framework would uncover additional separation points, though this extension lies beyond the present scope.

All 29 dimensions associated with T3 contribute equally from an information gain perspective, as each yielded identical accuracy in both training and testing. Nonetheless, they can be grouped into seven categories that differ considerably in their physical interpretation. These groups, detailed in Table 19, include parameters such as MSS (mass of stainless steel), MZR (mass of Zircalloy), MUO_2 (mass of uranium oxide), TSVC (local channel fluid temperature), TSS (stainless steel temperature), EFPD (total fission and decay heat energy), EMWR (oxidation energy), and DMH_2 (hydrogen mass from stainless steel, Zircalloy, and total production). Table 19 also specifies the spatial context of each parameter within the COR package of the MELCOR model, where Chen et al. [18] divided the core into 21 radial rings and 60 axial levels, with the active core corresponding to rings 1–15 and axial levels 40–60. In this notation, the first two digits indicate the ring number and the last two the axial level (e.g., 239 = ring 2, axial level 39; 1139 = ring 11, axial level 39).

Table 19. Breakdown of the 29 Dimensions Associated with T3. (Taken from Paper 5)

MSS	MZR	MUO2	TSVC	TSS	DMH2	Energy
239	140	140	201	810	SS	EFPD
339	240	240	202		ZIRC	EMWR
710	439		302		TOT	
838	539		504			
1139	1139		605			
1239	1239					
1339	1339					
	1439					
	1539					

This analysis concentrated on material masses, MSS, MZR, and MUO_2, which accounted for 18 of the 29 parameters extracted by DTIA. Of these, 12 were linked to axial level 39 (the layer directly below the core) and four to axial level 40 (the first level inside the core). As illustrated in Figure 37, MSS and MZR decreased to nearly zero around 17,500 seconds, marking the transition from T2 to T3. In the MELCOR model, axial level 39 represents the base of the Zircalloy canister; thus, these trends indicate the accumulation of molten material during T1 and T2, followed by its relocation downward as level 39 failed. This suggests near-complete canister failure and transfer of mass to the core support plate at axial level 38. Supporting evidence from Figure 38 shows UO_2 and Zircalloy relocation from level 40 to 39 at the same time. Notably, mass depletion occurred at different times across rings: inner rings (e.g., 2 and 3) failed later than outer rings (11–13). This pattern implies an outward-to-inward canister failure, consistent with the greater material mass in outer rings compared to the higher fission rate of inner rings. While plausible, this hypothesis requires further validation given uncertainties in MELCOR outputs. To examine this, MSS and MZR trends across all 15 core rings at axial level 39 were assessed (Figure 39). Rings 1–5 were the latest to reach zero, doing so closer to 20,000 seconds. The middle group of rings, however, showed less consistency, with anomalies such as rings 6 and 10 depleting later than expected relative to other rings in their group. These irregularities highlight that, although an outward-to-inward failure is strongly suggested, variations among individual rings must be considered before drawing definitive conclusions.

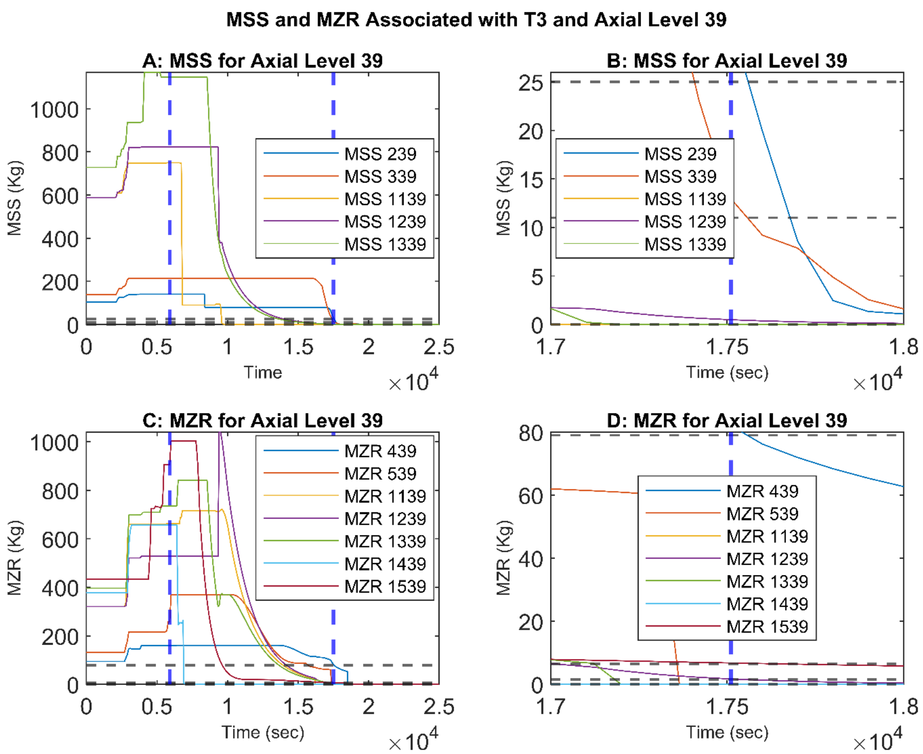

Figure 37. MSS and MZR at Axial Level 39, Separating T3 from T1 and T2. B and D are Zoomed Versions of A and C, Respectively. (Taken from Paper 5)

The analysis of depth 1, which corresponds to separating T1 from T2, revealed 94 dimensions strongly associated with this distinction, including 62 mass-related parameters (11 MSS, 25 MZR, and 26 MUO2) as listed in Table 20.

Additional parameters included MSSOX (stainless steel oxide mass) and particulate debris masses of UO_2 (PD_MUO2 and PB_MUO2). Many of these dimensions were linked to axial levels below the core support plate, indicating the early presence of MZR and MUO2 in this region, as shown in Figure 40. Although the detected masses were small, they suggest the onset of core support plate failure around 5900 seconds. This aligns partially with Yangli Chen et al., who reported failure at 6200 seconds, with the 300-second discrepancy warranting further investigation [63].

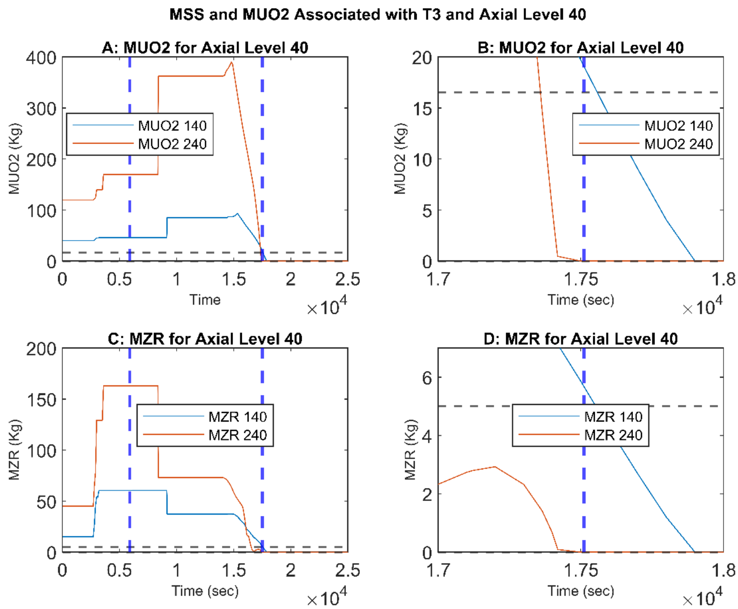

Figure 38. MUO2 and MZR at Axial Level 40, Separating T3 from T1 and T2. B and D are the Zoomed Versions of A and C, Respectively. (Taken from Paper 5)

The core support plate, represented in MELCOR as axial level 38, was examined through MSS, MZR, and MUO2 parameters from Table 20 to test the link between the 5900-second mark and support plate failure (Figure 41. A–C). These variables did not directly confirm plate failure at that time, as they showed sharp increases consistent with relocation from higher levels (e.g., axial level 39). However, the marked rise in MSS, MZR, and MUO2 at 5900 seconds points to significant canister failure, with Table 20 further highlighting a strong correlation between MUO2 at axial level 46 and this timestamp. Supporting evidence in Figure 41.D shows UO_2 masses across all rings dropping to zero by

5900 seconds. Taken together, these findings suggest that by this time, a significant amount of the core fuel had relocated to lower axial levels.

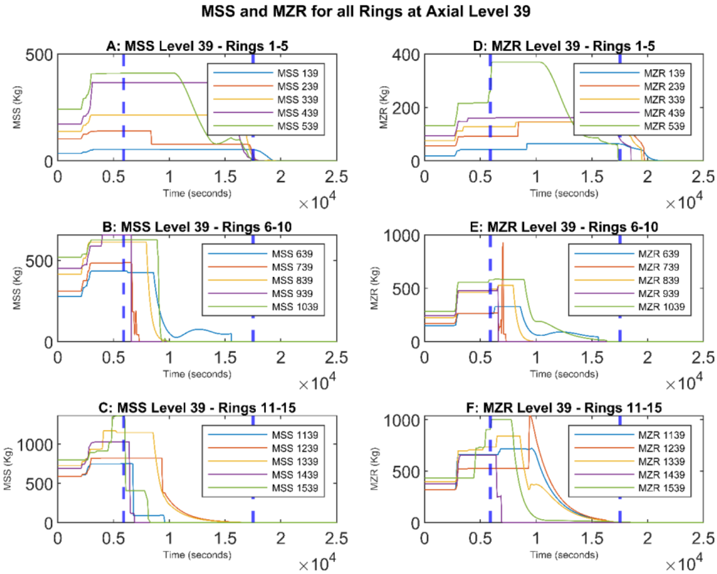

Figure 39. MSS and MZR for all Core Rings at Axial Level 39. (Taken from Paper 5)

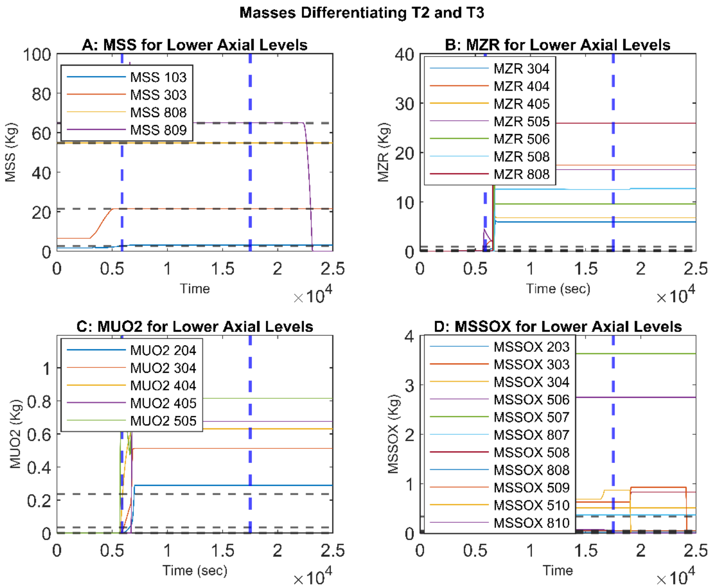

Figure 40. MSS, MZR, MUO2 and MSSOX for Lowest Axial Levels separating T1 from T2. (Taken from Paper 5)

Table 20. Breakdown of the 94 Dimensions Associated with Separating T1 from T2. (Taken from Paper 5)

MSS	**MSSOX**	**MZR**	**MUO2**	**PD_MUO2**	**PB_MUO2**	**TSS**	**TSVC**	**Totals**
103	203	304	204	1739	539	1138	838	EFPD
303	303	404	304	940	1739	1638	1641	EMWR
808	304	405	404	641	940		1642	DMH2_ZIRC
809	506	505	405	941	641			DMH2_SS
1211	507	506	505		941			
1212	807	508	1211					
538	508	808	1212					
1038	808	810	1213					
940	509	511	1313					
341	510	811	817					
441	810	1211	818					
	838	512	422					
	1038	1212	423					
		513	823					
		1213	826					
		1313	827					
		514	828					
		1414	538					
		422	1038					
		822	346					
		423	846					
		824	946					
		838	1046					
		1038	1146					
		541	1246					
			1546					

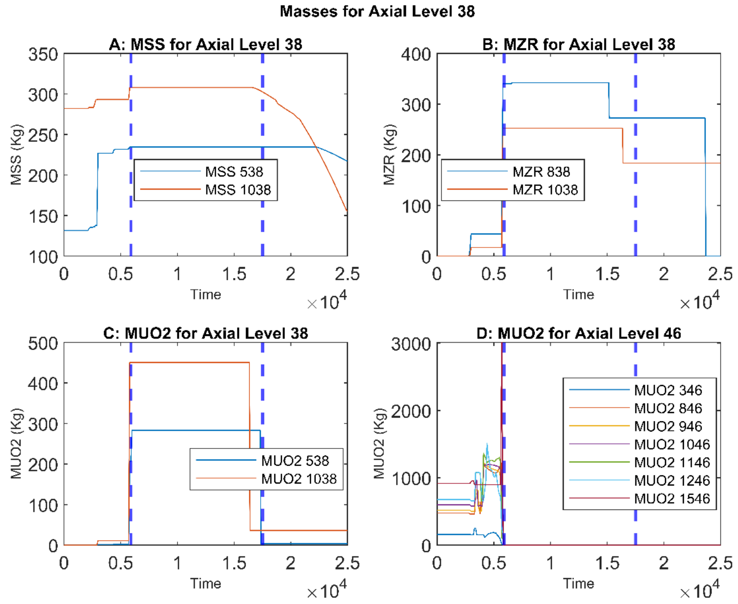

Figure 41. A, B, and C are MSS, MZR, and MUO2 for Axial Level 38, Separating T1 from T2, Respectively. D is MUO2 for Axial Level 46. (Taken from Paper 5)

4 Conclusion and Outlook

4.1 Conclusion

We demonstrated the potential of ML not only for developing predictive models that classify accident types, but also as an exploratory tool capable of uncovering distinctive insights into how accident scenarios differ over time through the evolution of their physical phenomena (first with the time and maximum external temperature of the reactor pressure vessel). Nevertheless, given the sensitivity and complexity of nuclear reactor safety (NRS), the insights generated by ML must be cross-validated by subject matter experts. Such insights can ultimately help subject matter experts gain a deeper understanding of the progression of accidents. While the first study focused on four accident scenarios and only two dimensions, it primarily served as a proof of concept to showcase the exploratory capacity of ML.

We introduced the generalised systematic pipeline of the developed Decision Tree Insights Analytics (DTIA) framework. DTIA builds on decision tree classifier (DTC) development to identify meaningful combinations of features and their associated thresholds in the feature space that show strong relationships with categorical target outputs. The framework is valid within the domain of classification problems and relies on the ability of DTCs to map input features to categorical outcomes. We demonstrated DTIA through three case studies. The first two highlighted its applicability in both physical and biological research contexts, while the third illustrated its limitations. In Case Study I, DTIA was shown to generate research questions that warrant further investigation, whereas Case Study II revealed novel biological insights. We compared the insights derived from DTIA against those provided by random forest feature importance and K-means feature ranking. Our results demonstrated that DTIA can deliver deeper and more interpretable insights into feature significance than these alternative approaches. Overall, DTIA validated certain findings reported in the literature and provided a structured means of identifying unexplored areas in the feature space that are strongly linked to categorical outputs, particularly in cases where researchers are uncertain about the associations they seek or are looking for further associations in the data to confirm or deny a hypothesis. Nonetheless, its effectiveness remains dependent on the DTC's mapping capability and on how the research problem is formulated. Finally, DTIA outperformed the random forest feature importance metric when evaluated using information gain calculations.

We applied DTIA to different case studies, first to the time-wise data of MELCOR's COR package results simulating an SBO + LOCA accident for a Nordic BWR and second, to the structural analysis results variables obtained from ANSYS FEA modelling of the RPV lower head at the time of failure due to the progression of two accidents: SBO and SBO + LOCA.

In the time-wise analysis application, we built upon the earlier modelling and traditional analysis conducted by Chen et al [63]. The prior analysis was used to define the labels (time windows) required for DTIA, enabling a systematic extraction of objective associations between COR package parameters and distinct time windows. This process significantly reduced the dataset's dimensionality, from 23,950 to 133 variables, while preserving the key associations of accident progression. Many of the extracted insights aligned with the established understanding of core degradation behaviour during severe accidents, thereby reinforcing the validity of the method. At the same time, DTIA uncovered previously unreported findings, including evidence that the core support plate does not fully melt within the first 90,000 seconds of accident progression, even after the pressure vessel fails. Additional insights raised new questions requiring further investigation, for instance, the observed increase in the mass of stainless steel and zircaloy prior to core support plate failure. It should be noted that tuning DTIA's hyperparameters is essential, as it directly influences the quality and reliability of the extracted insights. Overall, this study advances the pursuit of objectivity in severe accident analysis by removing the subjective step of pre-selecting parameters for investigation. Nonetheless, while DTIA provides an automated and structured approach to highlight meaningful correlations, the ultimate interpretation of these insights remains dependent on expert judgement.

In the structural analysis case study, we built upon the earlier modelling of the 2D RPV lower head ANSYS FEA model developed by Wang et al [73]. The model studied the structural behaviour through the two different accidents. Applying DTIA at the time of failure for both cases highlighted some insights that have been overlooked before, such as the compressive to tensile nodal solution ratio and how it can influence the mechanics of failure. These insights interpreted the findings of Wang et al. [73], showing why, in the case of the SBO + LOCA accident, the RPV lower head suffered more buckling and failed later than in the case of the SBO.

Finally, to introduce more objectivity to the proposed framework, we bootstrapped K-Means to DTIA, representing an evolution of the method. Whereas earlier DTIA studies relied on subject matter experts to pre-define the relevant time domains, the current framework objectively derives these domains through clustering. The framework employs K-Means clustering to partition time series variables from MELCOR into distinct time windows, which are subsequently analysed by DTIA to extract the most influential parameters associated with each domain. This combination revealed meaningful insights into SA progression, including the relocation of the core and the failure of the BWR canister, an event not highlighted in earlier traditional analyses of the same case. While the identified time windows did not always coincide with those recognised in traditional analysis, refinements such as hierarchical clustering may improve alignment. Furthermore, comparative studies remain necessary to cross-validate the extracted insights, and expert interpretation is still indispensable in assessing their physical relevance.

In summary, this work demonstrated the potential of machine learning not only as a predictive tool for accident classification but also as an exploratory framework capable of uncovering distinctive insights into accident progression. Through the development of the Decision Tree Insights Analytics (DTIA) framework, we systematically extracted meaningful features and threshold associations and applied the method across multiple domains, highlighting both its applicability and limitations. Applied to MELCOR's COR package results, DTIA substantially reduced the dimensionality of the dataset while preserving essential accident progression behaviour, uncovering previously unreported phenomena such as the incomplete melting of the core support plate and the rise of structural materials prior to failure. Similarly, when applied to structural analysis results, DTIA provided novel insights into the mechanics of reactor pressure vessel failure. Building on these applications, we evolved the framework by bootstrapping K-Means to DTIA, enabling objective identification of time domains that were previously defined by subject matter experts. This advancement reduced subjectivity and revealed further insights, such as canister failure, that were overlooked in traditional analyses. While the ultimate interpretation of the extracted insights remains dependent on expert judgment, the framework presented here represents a significant step toward objectively complementing the subjectivity of subject matter experts, enhancing scalability, and improving understanding in severe accident analysis.

4.2 Outlook

The research presented in this dissertation can be extended in two different dimensions: 1) extending the application of DTIA and other machine learning explainability techniques to other accident analyses, and 2) to further develop the bootstrapped DTIA with clustering for more objective insights extraction.

DTIA still needs to be extensively tested across various components of severe accident computations, including thermal hydraulics, containment phenomena, radionuclide production, and environmental radioactive release and propagation. Alongside the core relocation and degradation, aggregating all the insights extracted from applying DTIA to all packages can be challenging and needs further methodological development.

Bootstrapping DTIA to K-Means clustering revealed some insights, but it wasn't able to capture the traditional insights. Hence, it still requires some development to achieve better resolution in capturing time windows. That said, one approach would be to use hierarchical clustering in conjunction with a feature elimination step, which would provide more detailed time windows, leading to more objective insights.

References

1. Pavlakovič, B. Visiting nuclear reactors–Safety and security aspects. *International Journal of Thermofluids* **16**, (2022).
2. Gu, Z. History review of nuclear reactor safety. *Annals of Nuclear Energy* vol. 120 Preprint at https://doi.org/10.1016/j.anucene.2018.06.023 (2018).
3. Silva, K., Okamoto, K., Ishiwatari, Y., Takahara, S. & Promping, J. Consideration of decontamination model for severe accident consequence assessment. *J Nucl Sci Technol* **52**, (2015).
4. Hummel, D. W., Chouhan, S., Lebel, L. & Morreale, A. C. Radiation dose consequences of postulated limiting accidents in small modular reactors to inform emergency planning zone size requirements. *Ann Nucl Energy* **137**, (2020).
5. Nowobilski, T. & Hoła, B. Methodology based on causes of accidents for forcasting the effects of falls from scaffoldings using the construction industry in poland as an example. *Saf Sci* **157**, (2023).
6. Song, J. H., An, S. M., Kim, T. & Ha, K. S. Post-Fukushima challenges for the mitigation of severe accident consequences. *Nuclear Engineering and Technology* **52**, (2020).
7. Chen, G. W., Liang, H. C., Wang, W. S., Wang, T. C. & Wu, S. C. On-site simulator-based initiating event detection and identification in NPPs. *Progress in Nuclear Energy* **156**, (2023).

8. Zhao, F. *et al.* Safety analysis of marine nuclear reactor in severe accident with dynamic fault trees based on cut sequence method. *Nuclear Engineering and Technology* **54**, (2022).

9. Luo, R., Revankar, S. T., Zhang, D. & Zhao, F. Inherent Safety Characteristics of Lead Bismuth Eutectic-Cooled Accelerator Driven Subcritical Systems. *Front Energy Res* **10**, (2022).

10. Narendran, Y., Natesan, K., Devan, K. & John Arul, A. Analysis of unprotected loss of flow accident in a sodium cooled fast reactor using coupled thermal hydraulics neutronics code ASTRA. *Progress in Nuclear Energy* **163**, (2023).

11. Uchibori, A. *et al.* Numerical simulation technologies for safety evaluation in plant lifecycle optimization method, ARKADIA for advanced reactors. *Nuclear Engineering and Design* **413**, (2023).

12. Akbas, S., Quiroga, V. M., Aydogan, F., Allison, C. & Ougouag, A. M. Thermal-hydraulics and neutronic code coupling for RELAP/SCDAPSIM/MOD4.0. *Nuclear Engineering and Design* **344**, (2019).

13. Dwivedi, D. K., Gupta, A. & Kannan, U. Coupled neutronics–thermal-hydraulics analyses of unprotected transients in LBE-cooled Compact High-Temperature Reactor. *Life Cycle Reliability and Safety Engineering* **12**, (2023).

14. Wang, Z., Wang, G., Gu, Z., Jin, M. & Zhao, Z. Preliminary simulation of fuel dispersion in a Lead-Bismuth Eutectic (LBE)-cooled research reactor. *Progress in Nuclear Energy* **85**, (2015).

15. Li, G. *et al.* A review on MPS method developments and applications in nuclear engineering. *Computer Methods in Applied Mechanics and Engineering* vol. 367 Preprint at https://doi.org/10.1016/j.cma.2020.113166 (2020).

16. Miwa, S., Yamamoto, Y. & Chiba, G. Research activities on nuclear reactor physics and thermal-hydraulics in Japan after Fukushima-Daiichi accident. *Journal of Nuclear Science and Technology* vol. 55 Preprint at https://doi.org/10.1080/00223131.2017.1417177 (2018).

17. Paladino, D. *et al.* PANDA experimental database and further needs for containment analyses. *Nuclear Engineering and Design* **404**, (2023).

18. Silde, A., Ylijoki, J. & Ahtinen, E. Containment model library of the Apros process simulation software: an overview of development and validation work. *Progress in Nuclear Energy* **116**, (2019).

19. Kataoka, I. Review of thermal-hydraulic researches in severe accidents in light water reactors. *Journal of Nuclear Science and Technology* vol. 50 Preprint at https://doi.org/10.1080/00223131.2013.750797 (2013).

20. Manara, D. *et al.* Laser-heating and radiance spectrometry for the study of nuclear materials in conditions simulating a nuclear power plant accident. *Journal of Visualized Experiments* **2017**, (2017).

21. Pham, H. V., Kurata, M. & Steinbrueck, M. Steam Oxidation of Silicon Carbide at High Temperatures for the Application as Accident Tolerant Fuel Cladding, an Overview. *Thermo* vol. 1 Preprint at https://doi.org/10.3390/thermo1020011 (2021).

22. Pasi, A. E. *et al.* Gas phase interactions between tellurium and organic material in severe nuclear accident scenarios. *Ann Nucl Energy* **197**, (2024).

23. Kondo, T. *et al.* Thermophysical properties of molten $(Fe_2O_3)_{0.95}$-$(SiO_2)_{0.05}$ measured by aerodynamic levitation. *High Temp High Press* **53**, (2023).

24. Kurata, M., Okuzumi, N., Nakayoshi, A., Ikeuchi, H. & Koyama, S. Step-by-step challenge of debris characterization for the decommissioning of Fukushima-Daiichi Nuclear Power Station (FDNPS). *Journal of Nuclear Science and Technology* vol. 59 Preprint at https://doi.org/10.1080/00223131.2022.2040393 (2022).

25. Cho, J., Lee, S. H., Bang, Y. S., Lee, S. & Park, S. Y. Exhaustive simulation approach for severe accident risk in nuclear power plants: OPR-1000 full-power internal events. *Reliab Eng Syst Saf* **225**, (2022).

26. Zhao, N., Ma, W. & Bechta, S. A review of the assessment of severe accident management guidelines and actions through analytical simulations. *Annals of Nuclear Energy* vol. 180 Preprint at https://doi.org/10.1016/j.anucene.2022.109448 (2023).

27. Espinosa-Paredes, G., Camargo-Camargo, R. & Nuñez-Carrera, A. Severe accident simulation of the laguna verde nuclear power plant. *Science and Technology of Nuclear Installations* **2012**, (2012).

28. Cho, J., Lee, S. S. H., Bang, Y. S., Lee, S. S. H. & Park, S. Y. Exhaustive Simulation Approach for Severe Accident Risk in Nuclear Power Plants. *Reliab Eng Syst Saf* **225**, (2022).

29. Qiu, J. *et al.* MELCOR simulation of the SBLOCA induced severe accident for the SMR in a floating nuclear power plant. *Progress in Nuclear Energy* **129**, (2020).

30. Cervenka, J., Janda, Z., Jendele, L., Pukl, R. & Cervenka, V. Simulation of Severe Accident Scenarios in Nuclear Containments. in *Procedia Engineering* vol. 210 (2017).

31. Inagaki, K. Multi-physics particle method for the simulation of severe accidents in nuclear power plants. *Transactions of the Atomic Energy Society of Japan* **14**, (2015).

32. Nichenko, S., Kalilainen, J., Fernandez Moguel, L. & Lind, T. Modelling of fission products release in VERDON-1 experiment with cGEMS: Coupling of severe accident code MELCOR with GEMS thermodynamic modelling package. *Ann Nucl Energy* **152**, (2021).

33. Wang, H. *et al.* A hybrid fault diagnosis methodology with support vector machine and improved particle swarm optimization for nuclear power plants. *ISA Trans* **95**, 358–371 (2019).

34. Wang, H. *et al.* Fault identification and diagnosis based on KPCA and similarity clustering for nuclear power plants. *Ann Nucl Energy* **150**, (2021).

35. Liu, J., Seraoui, R., Vitelli, V. & Zio, E. Nuclear power plant components condition monitoring by probabilistic support vector machine. *Ann Nucl Energy* **56**, 23–33 (2013).

36. Zhao, Y., Tong, J., Zhang, L. & Wu, G. Diagnosis of operational failures and on-demand failures in nuclear power plants: An approach based on dynamic Bayesian networks. *Ann Nucl Energy* **138**, (2020).

37. Chae, Y. H., Kim, S. G., Kim, H. M., Kim, J. T. & Seong, P. H. A methodology for diagnosing FAC induced pipe thinning using accelerometers and deep learning models. *Ann Nucl Energy* **143**, (2020).

38. Nicolau, A. D. S., Augusto, J. P. D. S. C. & Schirru, R. Accident diagnosis system based on real-time decision tree expert system. in *AIP Conference Proceedings* vol. 1836 (American Institute of Physics Inc., 2017).

39. Jamil, F., Abid, M., Haq, I., Khan, A. Q. & Iqbal, M. Fault diagnosis of Pakistan Research Reactor-2 with data-driven techniques. *Ann Nucl Energy* **90**, 433–440 (2016).

40. Mandal, S., Santhi, B., Sridhar, S., Vinolia, K. & Swaminathan, P. A novel approach for fault detection and classification of the thermocouple sensor in Nuclear Power Plant using Singular Value Decomposition and Symbolic Dynamic Filter. *Ann Nucl Energy* **103**, 440–453 (2017).

41. Peng, B. Sen *et al.* Research on intelligent fault diagnosis method for nuclear power plant based on correlation analysis and deep belief network. *Progress in Nuclear Energy* **108**, 419–427 (2018).

42. Yu, Y., Peng, M. jun, Wang, H., Ma, Z. guo & Li, W. Improved PCA model for multiple fault detection, isolation and reconstruction of sensors in nuclear power plant. *Ann Nucl Energy* **148**, (2020).

43. Meng, J., Su, Y. & Xie, S. Loose parts detection method combining blind deconvolution with support vector machine. *Ann Nucl Energy* **149**, (2020).

44. Ayodeji, A. & Liu, Y. kuo. SVR optimization with soft computing algorithms for incipient SGTR diagnosis. *Ann Nucl Energy* **121**, 89–100 (2018).

45. Li, J. & Lin, M. Ensemble learning with diversified base models for fault diagnosis in nuclear power plants. *Ann Nucl Energy* **158**, (2021).

46. Hadad, K., Pourahmadi, M. & Majidi-Maraghi, H. Fault diagnosis and classification based on wavelet transform and neural network. *Progress in Nuclear Energy* **53**, 41–47 (2011).

47. Kim, M. *et al.* RNN-Based online anomaly detection in nuclear reactors for highly imbalanced datasets with uncertainty. *Nuclear Engineering and Design* **364**, (2020).

48. Vaddi, P. K. *et al.* Dynamic bayesian networks based abnormal event classifier for nuclear power plants in case of cyber security threats. *Progress in Nuclear Energy* **128**, (2020).

49. Mo, K., Lee, S. J. & Seong, P. H. A dynamic neural network aggregation model for transient diagnosis in nuclear power plants. *Progress in Nuclear Energy* **49**, 262–272 (2007).

50. Mohapatra, D., Subudhi, B. & Daniel, R. Real-time sensor fault detection in Tokamak using different machine learning algorithms. *Fusion Engineering and Design* **151**, (2020).

51. Hussein, S. M. & Demazière, C. Machine learning-based noise diagnostics for water-cooled SMRs: proof of principle on 2-dimensional systems. *Progress in Nuclear Energy* **189**, (2025).

52. Hegazy, A. H., Skoy, V. R. & Hossny, K. Optimization of Shielding-Collimator Parameters for ING-27 Neutron Generator Using MCNP5. in *EPJ Web of Conferences* vol. 177 (2018).

53. Abdelnour, M. R. *et al.* Prompt gamma neutron activation analysis: A review of applications, design, analytics, challenges, and prospects. *Radiation Physics and Chemistry* **234**, 112693 (2025).

54. Hossny, K., Hossny, A. H., Magdi, S., Soliman, A. Y. & Hossny, M. Detecting shielded explosives by coupling prompt gamma neutron activation analysis and deep neural networks. *Sci Rep* **10**, (2020).

55. Hossny, K., Magdi, S., Soliman, A. Y. & Hossny, A. H. Detecting explosives by PGNAA using KNN Regressors and decision tree classifier: A proof of concept. *Progress in Nuclear Energy* **124**, (2020).

56. Felix, E. A. & Lee, S. P. Systematic literature review of preprocessing techniques for imbalanced data. *IET Software* vol. 13 Preprint at https://doi.org/10.1049/iet-sen.2018.5193 (2019).

57. Minka, T. P. Automatic choice of dimensionality for PCA. in *Advances in Neural Information Processing Systems* (2001).

58. Oja, E. & Hyvarinen, A. Independent component analysis : algorithms and applications. *Neural Networks* **13**, (2000).

59. Martinez, A. M. & Kak, A. C. PCA versus LDA. *IEEE Trans Pattern Anal Mach Intell* **23**, (2001).

60. Lisboa, P. J. G., Saralajew, S., Vellido, A., Fernández-Domenech, R. & Villmann, T. The coming of age of interpretable and explainable machine learning models. *Neurocomputing* **535**, (2023).

61. Gauntt, R. O. *et al.* MELCOR Computer Code Manuals. *NUREG/CR-6119, Rev. 2* **1**, (2000).

62. Gauntt, R. O. *et al. MELCOR Computer Code Manuals - Vol.1: Primer and Users' Guide. NUREG/CR-6119, Rev. 2* vol. 1 (2017).

63. Chen, Y., Zhang, H., Villanueva, W., Ma, W. & Bechta, S. A sensitivity study of MELCOR nodalization for simulation of in-vessel severe accident progression in a boiling water reactor. *Nuclear Engineering and Design* **343**, (2019).

64. Chailan, L. *et al.* Overview of ASTEC integral code status and perspectives. *The 9TH European Review Meeting on Severe Accident Research (ERMSAR2019)* (2019).

65. Abobakr, A., Hossny, M., Abdelkader, H. & Nahavandi, S. RGB-D Fall Detection via Deep Residual Convolutional LSTM Networks. in *2018 International Conference on Digital Image Computing: Techniques and Applications, DICTA 2018* (2019). doi:10.1109/DICTA.2018.8615759.

66. Vicente-Valdez, P., Bernstein, L. & Fratoni, M. Nuclear data evaluation augmented by machine learning. *Ann Nucl Energy* **163**, (2021).

67. Galib, S. M., Bhowmik, P. K., Avachat, A. V. & Lee, H. K. A comparative study of machine learning methods for automated identification of radioisotopes using NaI gamma-ray spectra. *Nuclear Engineering and Technology* **53**, (2021).

68. Lu, Q. *et al.* Prediction method for thermal-hydraulic parameters of nuclear reactor system based on deep learning algorithm. *Appl Therm Eng* **196**, (2021).

69. Huang, Q. *et al.* A review of the application of artificial intelligence to nuclear reactors: Where we are and what's next. *Heliyon* vol. 9 Preprint at https://doi.org/10.1016/j.heliyon.2023.e13883 (2023).

70. Loktionov, V., Lyubashevskaya, I., Sosnin, O. & Terentyev, E. Short-term strength properties and features of high-temperature deformation of VVER reactor pressure vessel steel 15Kh2NMFA-A within the temperature range 20–1200 °C. *Nuclear Engineering and Design* **352**, (2019).

71. Wang, H., Villanueva, W., Chen, Y., Kulachenko, A. & Bechta, S. Thermo-mechanical behavior of an ablated reactor pressure vessel wall in a Nordic BWR under in-vessel core melt retention. *Nuclear Engineering and Design* **379**, (2021).

72. Yue, Y., Villanueva, W., Wang, H. & Wang, D. Thermo-mechanical analysis of instrumentation guide tube failure during a severe accident in

a nordic boiling water reactor. in *International Conference on Nuclear Engineering, Proceedings, ICONE* vol. 1 (2020).

73. Wang, H. D., Chen, Y. L. & Villanueva, W. Vessel Failure Analysis of a Boiling Water Reactor During a Severe Accident. *Front Energy Res* **10**, (2022).

74. Park, R. J., Kang, K. H., Hong, S. W. & Kim, H. Y. Detailed evaluation of melt pool configuration in the lower plenum of the APR1400 reactor vessel during severe accidents. *Ann Nucl Energy* **75**, (2015).

75. Mangalathu, S., Hwang, S. H. & Jeon, J. S. Failure mode and effects analysis of RC members based on machine-learning-based SHapley Additive exPlanations (SHAP) approach. *Eng Struct* **219**, (2020).

76. Ferreira, F. P. V., Shamass, R., Limbachiya, V., Tsavdaridis, K. D. & Martins, C. H. Lateral–torsional buckling resistance prediction model for steel cellular beams generated by Artificial Neural Networks (ANN). *Thin-Walled Structures* **170**, (2022).

77. Zakir Sarothi, S., Sakil Ahmed, K., Imtiaz Khan, N., Ahmed, A. & Nehdi, M. L. Predicting bearing capacity of double shear bolted connections using machine learning. *Eng Struct* **251**, (2022).

78. Thai, H. T. Machine learning for structural engineering: A state-of-the-art review. *Structures* vol. 38 Preprint at https://doi.org/10.1016/j.istruc.2022.02.003 (2022).

79. Li, C., Li, M. & Qiu, Z. An Unsupervised Learning-Based Framework for Effective Representation Extraction of Reactor Accidents. in *Springer Proceedings in Physics* vol. 284 SPPHY (2023).

80. Hossny, K., Villanueva, W. & Wang, H. D. Distinctive physical insights driven from machine learning modelling of nuclear power plant severe accident scenario propagation. *Sci Rep* **13**, (2023).

81. Hossny, K., Hossny, M., Cougnoux, A., Mahmoud, L. & Villanueva, W. Decision tree insights analytics (DTIA) tool: an analytic framework to identify insights from large data records across fields of science. *Mach Learn Sci Technol* **5**, 045004 (2024).

82. Hossny, K. & Villanueva, W. Analysing nuclear reactor severe accident time-wise propagation stages using DTIA. in *ANS Annual Conference 2025* (American Nuclear Society (ANS), Chicago, USA, 2025). doi:doi.org/10.13182/T140-48396.

83. Cougnoux, A. *et al.* Single cell transcriptome analysis of niemann–pick disease, type c1 cerebella. *Int J Mol Sci* **21**, (2020).

84. Cougnoux, A. *et al.* Toll-like receptor mediated lysozyme expression in Niemann-pick disease, type C1. *Mol Genet Metab* **131**, (2020).

85. Maulik, M. *et al.* Mutant human APP exacerbates pathology in a mouse model of NPC and its reversal by a β-cyclodextrin. *Hum Mol Genet* **21**, (2012).

86. Kelić, S., Levy, S., Suarez, C. & Weinstein, D. E. CD81 regulates neuron-induced astrocyte cell-cycle exit. *Molecular and Cellular Neuroscience* **17**, (2001).

87. Cougnoux, A. *et al.* Microglia activation in Niemann-Pick disease, type C1 is amendable to therapeutic intervention. *Hum Mol Genet* **27**, (2018).

88. Orthgiess, J. *et al.* Neurons exhibit Lyz2 promoter activity in vivo: Implications for using LysM-Cre mice in myeloid cell research. *Eur J Immunol* **46**, (2016).

89. Keren-Shaul, H. *et al.* A Unique Microglia Type Associated with Restricting Development of Alzheimer's Disease. *Cell* **169**, (2017).

90. Gospodarowicz, M. *et al.* History and international developments in cancer staging. *Cancer prevention & control : CPC = Prévention & contrôle en cancérologie : PCC* vol. 2 Preprint at (1998).

91. Sobin, L. H. TNM: Evolution and relation to other prognostic factors. *Seminars in Surgical Oncology* vol. 21 Preprint at https://doi.org/10.1002/ssu.10014 (2003).

92. Weiss, A. *et al.* Validation study of the American joint committee on cancer eighth edition prognostic stage compared with the anatomic stage in breast cancer. *JAMA Oncol* **4**, (2018).

93. Weinstein, J. N. *et al.* The cancer genome atlas pan-cancer analysis project. *Nat Genet* **45**, (2013).

94. Li, X., Masliah, E., Reixach, N. & Buxbaum, J. N. Neuronal production of transthyretin in human and murine alzheimer's disease: Is it protective? *Journal of Neuroscience* **31**, (2011).

95. Eckhardt, C. M. *et al.* Unsupervised machine learning methods and emerging applications in healthcare. *Knee Surgery, Sports*

Traumatology, Arthroscopy vol. 31 Preprint at https://doi.org/10.1007/s00167-022-07233-7 (2023).

96. Jain, A. K. Data clustering: 50 years beyond K-means. *Pattern Recognit Lett* **31**, (2010).

97. Ahmed, M., Seraj, R. & Islam, S. M. S. The k-means algorithm: A comprehensive survey and performance evaluation. *Electronics (Switzerland)* vol. 9 Preprint at https://doi.org/10.3390/electronics9081295 (2020).